ACS OMEGA

Open Access

This article is licensed under CC-BY-NC-ND 4.0

http://pubs.acs.org/journal/acsodf

Article

Novel 3,6-Disubstituted Pyridazine Derivatives Targeting JNK1 Pathway: Scaffold Hopping and Hybridization-Based Design, Synthesis, Molecular Modeling, and *In Vitro* and *In Vivo* Anticancer Evaluation

Mai M. Shaalan, Essam Eldin A. Osman, Yasmeen M. Attia, Olfat A. Hammam, Riham F. George,* and Bassem H. Naguib*

Cite This: *ACS Omega* 2024, 9, 37310−37329

Read Online

ACCESS | Metrics & More | Article Recommendations | Supporting Information

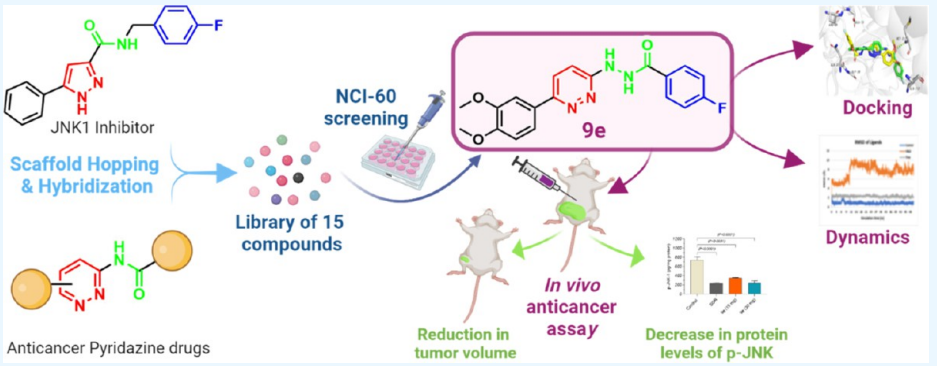

ABSTRACT: A series of novel 3,6-disubstituted pyridazine derivatives were designed, synthesized, and biologically evaluated as preclinical anticancer candidates. Compound **9e** exhibited the highest growth inhibition against most of the NCI-60 cancer cell lines. The *in vivo* anticancer activity of **9e** was subsequently investigated at two dose levels using the Ehrlich ascites carcinoma solid tumor animal model, where a reduction in the mean tumor volume allied with necrosis induction was reported without any signs of toxicity in the treated groups. Interestingly, compound **9e** was capable of downregulating c-jun N-terminal kinase-1 (JNK1) gene expression and curbing the protein levels of its phosphorylated form, in parallel with a reduction in its downstream targets, namely, c-Jun and c-Fos in tumors, along with restoring p53 activity. Furthermore, molecular docking and dynamics simulations were carried out to predict the binding mode of **9e** and prove its stability in the JNK1 binding pocket.

1. INTRODUCTION

Being the second cause of death worldwide, substantial efforts remain underway to develop therapeutic modalities for cancer with ample safety and efficacy profiles.[1] In addition to conventional chemotherapy, targeted therapy and immunotherapy have indeed enriched the therapeutic options for cancer patients to improve prognosis.[2] However, pressing paramount challenges to achieve the desired therapeutic outcomes from using conventional chemotherapy or immunotherapy are chemoresistance,[3] toxicity,[4] and poor response rates.[5] Given a better understanding of the molecular basis of cancer, there is an unceasing demand for targeted, more potent therapies that can overcome emerging resistance and toxicity. The tendency of kinases to activate multiple signaling pathways of cancer cell survival, proliferation, and metastasis has made them a promising molecular target for cancer treatment.[6]

C-jun N-terminal kinases (JNKs) belong to the mitogen-activated protein kinase (MAPK) family of serine-threonine kinases.[7] Also, JNKs are known as stress-activated protein kinases (SAPKs) that are triggered in response to radiation, environmental stress, and growth factors.[8] The JNK family consists of three proteins (JNK1, JNK2, and JNK3) that are encoded by three different genes *jnk1* (Mapk8), *jnk2* (Mapk9), and *jnk3* (Mapk10), respectively, and are alternatively spliced to produce at least ten variants.[9] While JNK1 and JNK2 are found in almost all tissues, JNK3 is only found in the brain, heart, and testes.[10] Upon the binding of JNK to a phosphate-donating molecule, typically adenosine triphosphate (ATP), JNK is phosphorylated and activated.[11] JNK then passes the

Received: June 4, 2024
Revised: August 11, 2024
Accepted: August 13, 2024
Published: August 19, 2024

© 2024 The Authors. Published by American Chemical Society

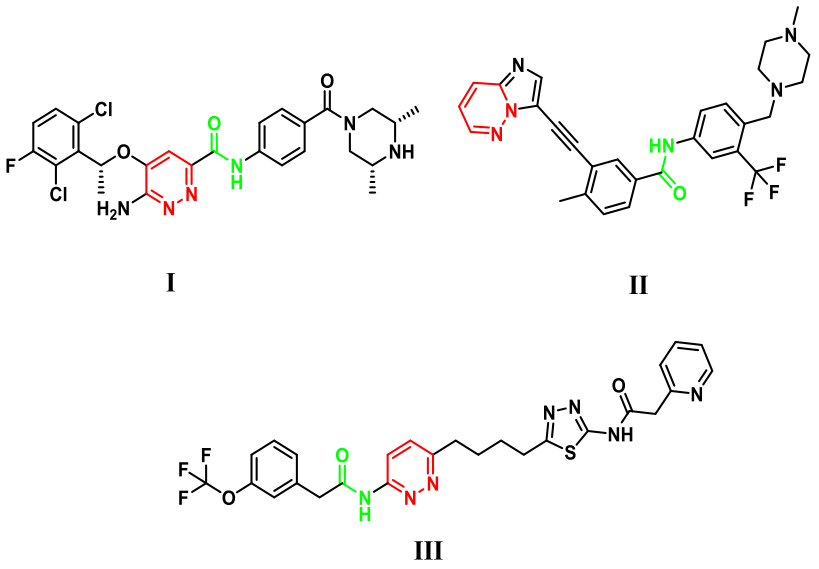

Figure 1. Some pyridazine-containing anticancer targeted inhibitors (I−III) with amide moieties.

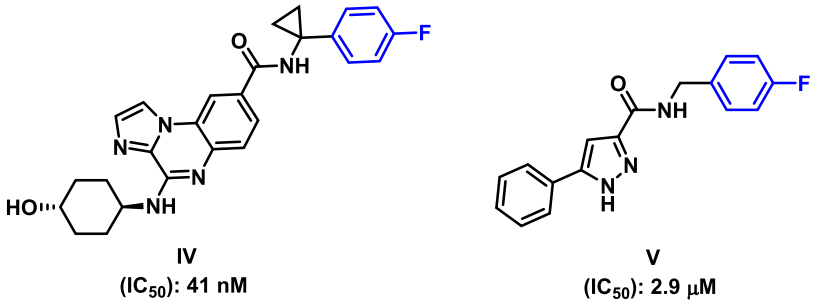

Figure 2. JNK1 inhibitors bearing a 4-fluorophenyl group.

signal by translocating from the cytosol to the nucleoplasm phosphorylating various transcription factors of the activator protein 1 (AP-1) family.[12] JNK activates AP-1 through phosphorylation of the transcription factor c-Jun, the prototypical downstream target of JNK.[13] The Ser63 and Ser73 phosphorylated c-Jun then heterodimerizes to c-fos, another member of the AP-1 family, forming a transcriptionally competent AP-1 complex.[14] Inhibiting c-Jun activity was reported to prevent colony formation and inhibit the proliferation of the MCF-7 breast cancer cell line.[15] Besides the activation of the AP-1 family, JNKs phosphorylate and activate a variety of nuclear and non-nuclear proteins, including c-Myc, activating transcription factor 2, NFAT, Elk1, and cell death regulators of the Bcl-2 family in the mitochondria.[10] It was also found that persistent activation of JNKs is involved in carcinogenesis and tumor progression.[16] In addition, JNK1 activation was found to downregulate the tumor suppressor p53 protein expression predisposing to a broad spectrum of cancers.[17,18] Besides, cyclin D1, another downstream target of the JNK pathway, was reported to drive proliferation through the induction of cell cycle progression.[19] These findings stimulate the need to design and synthesize chemical libraries of compounds that can act as JNK inhibitors.

The pyridazine nucleus has a broad range of biological activities including anticancer,[20−23] analgesic/anti-inflammatory,[24,25] antimicrobial,[26] antihypertensive,[27,28] and antifungal activities[29] and can also be utilized to link other pharmacophoric groups.[30] In addition, several pyridazine-containing targeted inhibitors with amide moieties (Figure 1) are now in clinical practice for the treatment of different cancers.[31−34] Ensartinib (**I**), an orally bioavailable tyrosine kinase inhibitor, has shown efficacy in patients with nonsmall cell lung cancer (NSCLC) targeting the anaplastic lymphoma kinase.[32] Ponatinib (**II**), an oral pan-inhibitor of breakpoint cluster region-Abelson kinase (BCR-ABL), is also used in chronic myeloid leukemia.[33] Telaglenastat (**III**), a selective glutaminase inhibitor, has demonstrated efficacy against triple-negative breast cancer (TNBC) and renal cell carcinoma (RCC).[31] These compounds acknowledge the fact that pyridazine derivatives exhibit favorable therapeutic potential in cancer.

In parallel, several compounds with varied heterocyclic rings were reported to have JNK1 inhibitory activity.[35−37] Surprisingly, JNK1 inhibitors **IV** and **V** bearing a 4-fluorophenyl group were found to possess exceptionally high inhibitory activity compared to other derivatives of the same series (Figure 2). This has been attributed to occupying an induced fit binding pocket in JNK1 formed by Glu73 and Arg69 that was not found in the apo structures of other JNK isoforms.[36,37]

Accordingly, the current study sought to design a series of novel target compounds based on the scaffold hopping of JNK1 inhibitor **V** by ring expansion of the pyrazole ring into a pyridazine ring and the bioisosteric replacement of the amide linker by hydrazide, semicarbazide, and thiosemicarbazide moieties. Additionally, the impact of hybridization between the pyridazine ring with its potent anticancer effect and the 4-

https://doi.org/10.1021/acsomega.4c05250
ACS Omega 2024, 9, 37310−37329

Scheme 1. Synthesis of Intermediate Compounds 5a,b[a]

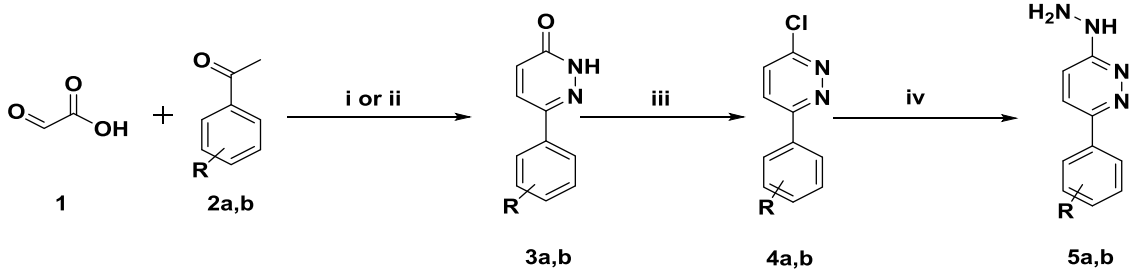

[a]Reagents and conditions: (i) acetophenone (**2a**), 110 °C, 2h; $NH_2NH_2.H_2O$, reflux, 2 h; (ii) 3′,4′-dimethoxyacetophenone (**2b**), acetic acid, reflux, 10 h; $NH_2NH_2.H_2O$ reflux, 2 h; (iii) $POCl_3$, 100 °C, 2 h; and (iv) $NH_2NH_2.H_2O$, 130 °C, 1 h.

Scheme 2. Synthesis of Target Compounds 7, 9a−g, and 11a−g[a]

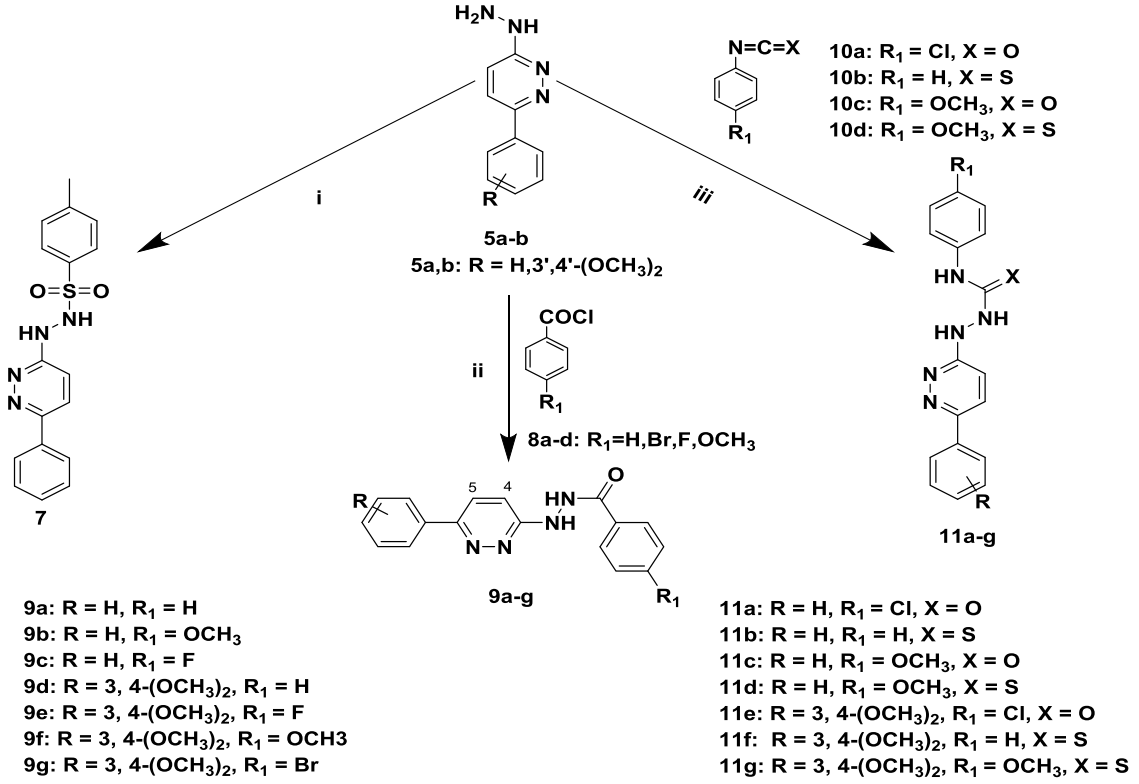

[a]Reagents and conditions: (i) 4-toluenesulfonyl chloride (**6**), DCM, TEA, rt, 3 h; (ii) Et_2O, TEA, rt, 1 h; and (iii) DCM, TEA, rt, 6 h.

fluorophenyl group responsible for the explicitly high JNK1 inhibitory activity was investigated. Afterward, the designed series of 3,6-disubstituted pyridazine derivatives were synthesized and screened against NCI-60 human tumor cell lines. The most active compound was then evaluated for its *in vivo* anticancer and JNK1 inhibitory activities. Finally, molecular docking and dynamics predicted and confirmed the binding mode of the most active compound *in silico*.

2. RESULTS AND DISCUSSION

2.1. Chemistry. The intermediate and target compounds' synthetic pathways are outlined in Schemes 1 and 2, respectively. First, glyoxylic acid (**1**) was reacted with acetophenones **2a,b**, followed by treatment with hydrazine hydrate to yield 6-substituted phenyl-3(2H)-pyridazinones **3a,b.**[38] Then, compounds **3a,b** were refluxed with phosphorus oxychloride to obtain 3-chloro-6-substituted phenyl pyridazines **4a,b**[39] that were then reacted with hydrazine hydrate to give 6-substituted phenylpyridazin-3-yl hydrazines **5a,b**[40] as illustrated in Scheme 1.

The IR spectra of compounds **5a,b** showed two bands of NH and NH_2 stretching vibrations at 3197−3560 cm^{-1}. ^1H NMR spectrum of **5b** revealed two singlet peaks of the hydrogens of methoxy groups at C-3 and C-4 in the phenyl ring at 3.80 and 3.84 ppm, along with two D_2O exchangeable broad singlet signals at 4.35 and 7.96 ppm corresponding to NH_2 and NH protons, respectively. The target compounds were obtained from the reaction of the appropriate 3-hydrazinylpyridazine derivatives **5a,b** with either 4-toluenesulfonyl chloride (**6**), substituted benzoyl chlorides **8a−d**, or

https://doi.org/10.1021/acsomega.4c05250
ACS Omega 2024, 9, 37310−37329

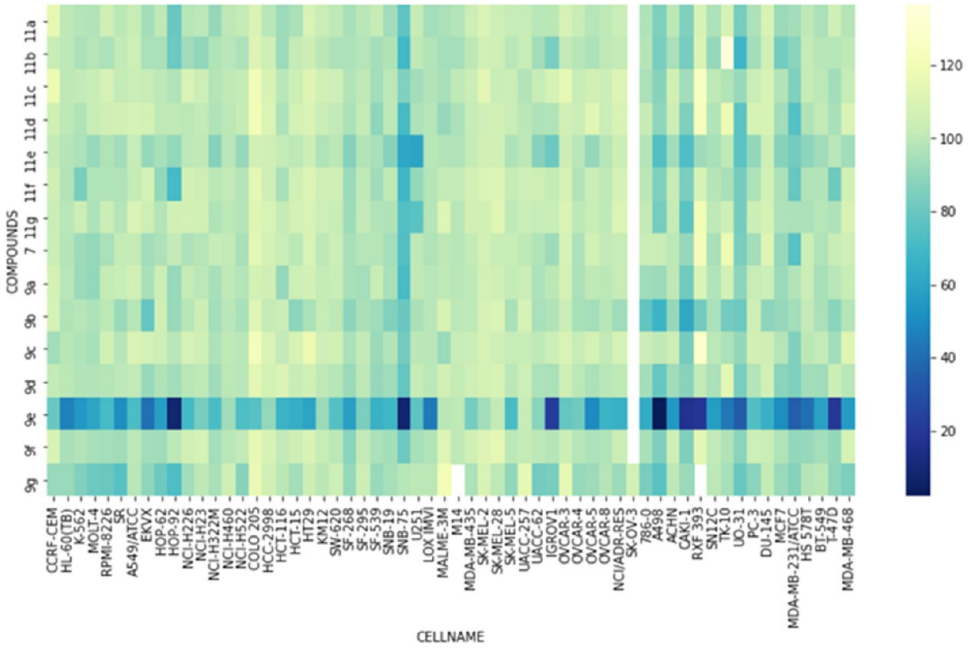

Figure 3. Heat map illustrating the growth percentage of compounds **7**, **9a−g**, and **11a−g** (*y*-axis) at a concentration of 10 μM against the NCI-60 cell lines (*x*-axis). The color ranges from dark blue (low growth %) to yellow color (high growth %).

substituted isocyanates and isothiocyanates **10a−d** (Scheme 2).

Compound **7** was prepared by the reaction of **5a** with 4-toluenesulfonyl chloride (**6**) in dichloromethane and triethylamine. The IR spectrum revealed the characteristic bands of the sulfonyl group at 1415 (forked peak) and 1165 cm^{-1}. Moreover, the ^{1}H NMR spectrum of compound **7** showed a singlet signal of a methyl group at 2.38 ppm together with two singlet signals at 9.17 and 9.92 ppm corresponding to two NH protons, which were exchanged with D_2O. In the ^{13}C NMR spectrum, the methyl group signal appeared at 21.5 ppm.

Compounds **9a−g** were obtained from the reaction of compounds **5a−b** with substituted benzoyl chlorides **8a−d** in diethyl ether and triethylamine. The structures of compounds **9a−g** were confirmed by the appearance of two bands of NH stretching vibrations at 3140−3506 cm^{-1}, as well as the carbonyl stretching vibrations at 1651−1681 cm^{-1} in the IR spectra. Moreover, ^{1}H NMR showed two broad, singlet signals of NH protons at 8.98−9.18 and 10.43−10.67 ppm that disappeared upon deuteration. In addition, a homogeneous pattern of pyridazine's protons was observed.

The pyridazine's proton at carbon 4 was detected with or without overlapping with another aromatic proton at 7.02−7.09 ppm. However, the other proton at carbon 5 appears downfield around 8.06−7.93 ppm with or without overlapping with other aromatic protons. The shielding of the pyridazine's proton at carbon 4 can be attributed to the + M effect of the hydrazino group. In ^{13}C NMR spectra, methoxy group signals appeared between 55.87 and 56.02 ppm and carbonyl group signals appeared between 166.21 and 166.90 ppm.

Finally, the reaction of 3-hydrazinylpyridazines **5a−b** with the appropriate isocyanates or isothiocyanates **10a−d** in dichloromethane and triethylamine yielded the target compounds **11a−g**. The IR spectra revealed the presence of the NH stretching vibration as three bands in the range of 3113−3332 cm^{-1}. Furthermore, the semicarbazide derivatives **11a**, **c**, and **e** showed carbonyl stretching vibrations at 1658−1674 cm^{-1}, while the thiosemicarbazide derivatives **11b**, **d**, **f**, and **g** showed thiocarbonyl stretching vibrations at 1219−1222 cm^{-1}. ^{1}H NMR spectra of semicarbazide derivatives **11a**, **c**, and **e** confirmed the obtained structures through the presence of three D_2O exchangeable, singlet peaks of NH hydrogens at 8.24−8.43, 8.75−8.93, and 8.88−9.10 ppm, respectively. On the other hand, thiosemicarbazide derivatives **11b**, **d**, **f**, and **g** showed more deshielded ranges for the corresponding three singlet peaks of NH protons at 9.11−9.25, 9.74−9.88, and 9.86−10.01 ppm due to increased magnetic anisotropy of the thiocarbonyl moiety resulting from the high polarizability of the thiocarbonyl bond.[41] Singlet peaks of the hydrogens of methoxy groups occur at 3.70−3.86 ppm. The homogeneous pattern of pyridazine's protons was also observed in this series. For ^{13}C NMR spectra, methoxy group signals were detected between 55.59 and 56.05 ppm. Additionally, the semicarbazide derivatives **11a**, **c**, and **e** showed carbonyl group signals between 160.37 and 160.92 ppm, while the thiosemicarbazide derivatives **11b**, **d**, **f**, and **g** showed thiocarbonyl signals between 181.95 and 182.24 ppm.

2.2. *In Vitro* Antiproliferative Screening against NCI-60 Cell Lines. *2.2.1. NCI Single-Dose Testing.* All of the synthesized compounds **7**, **9a−g**, and **11a−g** were screened against NCI-60 human cancer cell lines by the Developmental Therapeutic Program (DTP), National Cancer Institute (NCI).[42] The tested compounds showed low to moderate inhibitory activity at a concentration of 10 μM (Figures S35−S49) except for compound **9e**, which demonstrated the highest growth inhibition percent against most of the 60 cell lines with a mean growth inhibition percentage of 37.91% (Figures 3 and S40).

Compound **9e** showed 53.12% inhibition on the leukemia cell line HL-60(TB), and 63.82, 58.88, and 79.98% inhibition on MDA-MB-231/ATCC, HS 578T, and T-47D breast cancer cell lines, respectively. Moreover, it exhibited 91.82, 55.80, and 77.88% inhibition on CNS SNB-75, Melanoma LOX IMVI, and ovarian cancer IGROV1 cell lines, respectively. Interest-

https://doi.org/10.1021/acsomega.4c05250
ACS Omega 2024, 9, 37310−37329

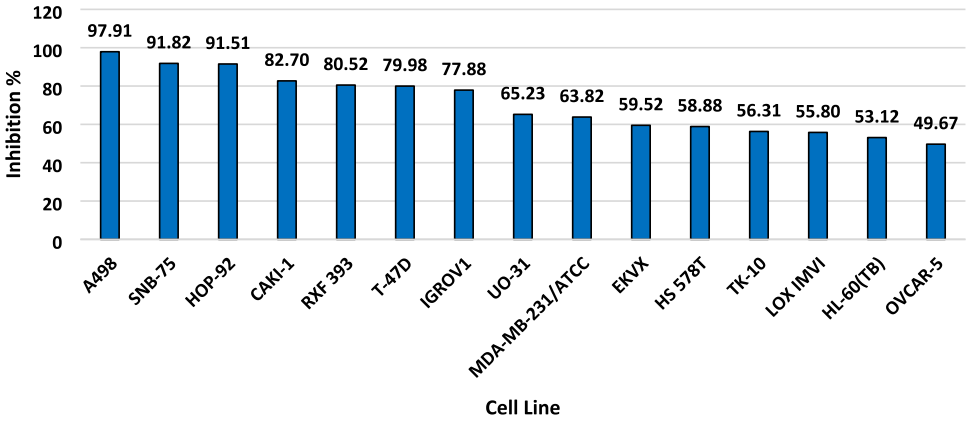

Figure 4. Growth inhibition percent of compound **9e** against the 15 most sensitive 15 cell lines from the NCI-60 cell lines that show a percent inhibition range from 49.67 to 97.91%.

ingly, **9e** showed superior inhibitory activity on renal and nonsmall cell lung cancer cell lines, where it demonstrated 97.91, 82.70, 80.52, 56.31, and 65.23% inhibition on A498, CAKI-1, RXF 393, TK-10, and UO-31 renal cancer cell lines, as well as 91.51 and 59.52% inhibition on HOP-92 and EKVX nonsmall cell lung cancer cell lines, respectively (Figure 4).

2.2.2. NCI Five-Dose Testing. Compound **9e** that demonstrated promising results in single-dose testing was then examined in a five-dose mode to assess the molar concentration required to cause 50% growth inhibition (GI_{50}) over all 60 human cancer cell lines representing the nine tumor subpanels. The 60 cell lines were incubated with five different concentrations of compound **9e** (0.01, 0.1, 1, 10, and 100 μM) (Table S1).

Compound **9e** showed significant antiproliferative activity against most of the cell lines evaluated with GI_{50} values in the micromolar range. As shown in Table 1, the overall highest activity was observed with the NSCLC subpanel, with a GI_{50} value of 17.8 μM on the HOP-92 cell line, followed by the breast, CNS, renal, and leukemia cancer subpanels (Figure S50).

Table 1. GI_{50} (μM) Values for Compound 9e against the Most Sensitive Cell Lines

panel/cell line	GI_{50} (μM)	panel/cell line	GI_{50} (μM)
leukemia		**ovarian cancer**	
CCRF-CEM	**38**	IGROV1	63.3
HL-60(TB)	**33.5**	OVCAR-3	79.7
K-562	58.7	OVCAR-4	55.3
MOLT-4	40.6	NCI/ADR-RES	43.2
RPMI-8226	**35.3**	**renal cancer**	
nonsmall cell lung cancer		CAKI-1	**34.3**
A549/ATCC	99.5	RXF 393	63
HOP-62	91.7	UO-31	**31.8**
HOP-92	**17.8**	**prostate cancer**	
NCI-H226	71.8	PC-3	50.6
NCI-H522	54.3	**breast cancer**	
colon cancer		MCF7	93.4
~~HCT-15~~	65.5	MDA-MB-231/ATCC	93
CNS cancer		HS 578T	63.9
SF-268	79.8	BT-549	**22.9**
SNB-75	**26.9**	T-47D	**28.1**
melanoma		MDA-MB-468	64.3
LOX IMVI	67.6		
SK-MEL-5	45		

Remarkably, the micromolar potency seen in the cellular-based assays of compound **9e** conforms with numerous previously reported ATP-competitive JNK inhibitors.[43−46] These studies showed that the relatively high ATP concentration in cells, rather than the limited cell penetration, might account for their micromolar cellular potency.[43−45] Cross-talk between cells in the tumor microenvironment seems to operate to account for the higher activity of some JNK inhibitors *in vivo* despite their moderate *in vitro results.*[47−49]

These findings, together with the fact that the phosphorylated JNK/c-Jun axis is specifically activated in multiple cancer cell lines and tissue samples,[50−56] have instigated the *in vivo* investigation of whether compound **9e** could exhibit its anticancer potential via JNK1 inhibition.

2.3. Evaluation of the *In Vivo* Anticancer Activity and Safety of 9e. The promising *in vitro* results of **9e** prompted further evaluation of its *in vivo* anticancer activity at two dose levels (15 and 30 mg/kg) in an Ehrlich ascites carcinoma (EAC) solid tumor animal model using Sorafenib (SOR) as a reference at a dose of 30 mg/kg. Sorafenib was chosen as a reference since it is a multiple kinase inhibitor with a well-known anticancer activity against different types of cancers including kidney, liver, breast, colon, NSCLC, and acute myelocytic leukemia.[57,58]

*2.3.1. Effect of **9e** on Body Weight and Its Overall Safety Profile on Multiple Organs.* As demonstrated in Figure 5A, there was no observed change in body weights among all of the animal groups. Moreover, neither mortality nor acute signs of toxicity were reported in the treated groups over the experimentation period. The animals' excitability and vitality were also normal. Additionally, to confirm the safety of compound **9e**, a histopathological examination of its effect on several organs was performed. As shown in Figure 6, H&E-stained liver sections from the **9e**-treated group showed normal hepatic architecture with hepatocytes appearing in thin plates and normal morphology and distribution of sinusoids. Moreover, **9e** did not show any notable changes in lung tissues, where normal alveoli with thin interalveolar septum and type I and type II pneumocytes were seen. Kidney sections also demonstrated renal cortex showing renal corpuscle with normal glomerulus and normal pattern of proximal and distal convoluted tubules with no remarkable differences from the untreated normal group. Additionally, H&E-stained heart

https://doi.org/10.1021/acsomega.4c05250
ACS Omega 2024, 9, 37310−37329

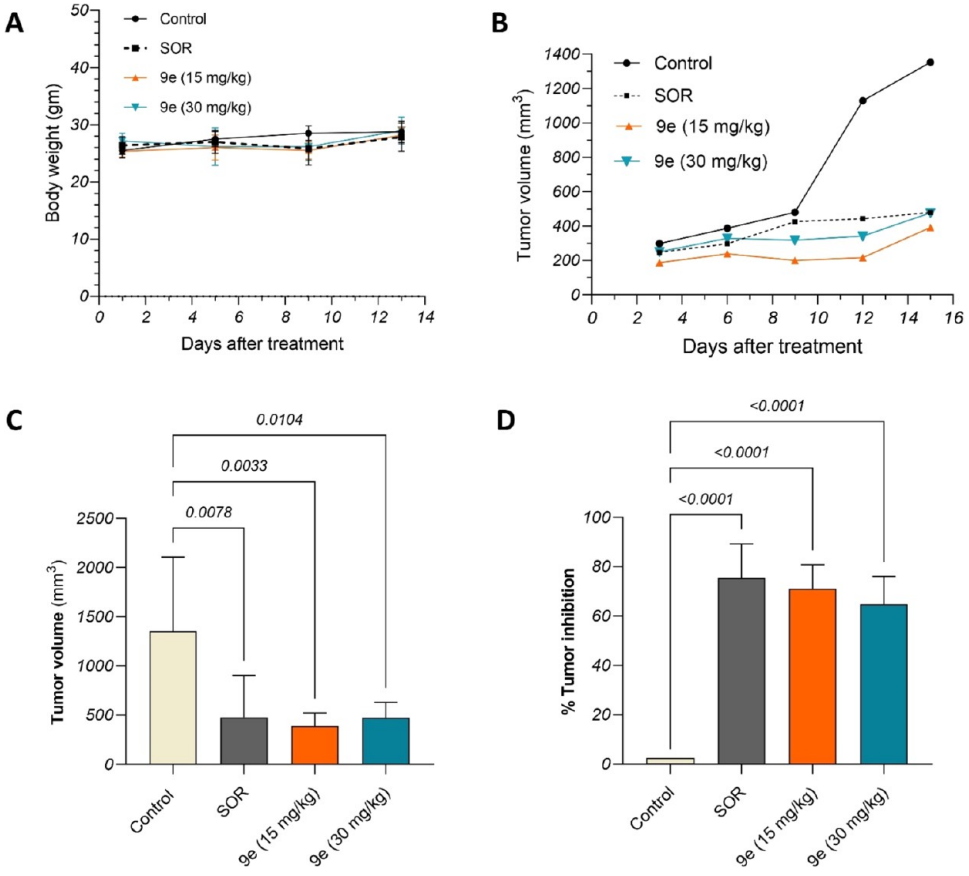

Figure 5. Effect of 9e on body weights and tumor volumes in EAC-bearing mice. (A) Body weights in control, SOR (30 mg/kg)-, **9e** (15 mg/kg)-, and **9e** (30 mg/kg)-treated groups. (B) Tumor volumes of mice belonging to control and treated groups, measured at 3, 6-, 9-, 12-, and 15-days post-treatment. Bar charts showing changes in tumor volumes in control and treated groups on day 15 post-treatment were represented as (C) tumor volumes (mm^3) and (D) tumor growth inhibition (%). Values are presented as mean ± SD. One-way ANOVA followed by Tukey's post hoc test was applied for statistical analysis. *P*-values less than 0.05 were considered statistically significant.

sections from the **9e**-treated group showed a normal morphological appearance with normal myocardial muscle fibers. Spleen sections also showed a normal morphological appearance with white and red pulps. Histological sections from the small intestine of the **9e**-treated group were also comparable to that from the normal group, where the mucosa was lined by columnar mucin-secreting cells with normal villous pattern and goblet cells, submucosal structure, and muscle layer. These results indicate the safety of **9e** on multiple organs; however, further toxicity studies are recommended to warrant further identification of potential adverse effects in humans.

*2.3.2. Effect of **9e** on Tumor Volumes.* Tumor volumes were recorded over fixed intervals to evaluate the anticancer activity of **9e** *in vivo*. Measurements were taken 3, 6, 9, 12, and 15 days after treatment initiation. Significant changes started to be evident on day 12, where **9e** (15 mg/kg) showed an 80.9% reduction in tumor volume, as compared to the control untreated group. On the 15th day, SOR (30 mg/kg), **9e** (15 mg/kg), and **9e** (30 mg/kg) demonstrated regressions in tumor volumes reaching 64.6, 71.1, and 64.8% from control, respectively (Figure 5**B**–**D**).

*2.3.3. Effect of **9e** on Histopathological Changes and Necrotic Indices.* Tumor sections from untreated control EAC-bearing mice demonstrated sheets of small and large malignant epithelial cells with enlarged nuclei and increased nucleocytoplasmic ratio with mitosis and with no areas of necrosis (Figure 7A,7B). The SOR-treated group, however, showed sheets of malignant cells with moderate areas of necrosis and apoptosis (Figure 7C). Tumor sections from mice treated with **9e** at a dose of 15 mg/kg showed small sheets of malignant cells, extensive necrosis, and multiple apoptotic bodies (Figure 7D). Additionally, as shown in Figure 7E, tumor sections from **9e** (30 mg/kg) displayed sheets of malignant cells, large areas of necrosis and apoptosis, multiple apoptotic bodies, and scattered macrophages. Regarding necrosis assessment in histological sections, treatment with SOR (30 mg/kg) caused an increase in the necrotic index reaching 42-fold compared to control, whereas **9e** at low and high doses elicited a 66- and a 72-fold upsurge in the mean index, as compared to the control untreated group, respectively. Interestingly, a high dose of **9e** depicted a significantly higher elevation in the necrotic index than that observed with SOR by 1.72 folds (Figure 7F). Accordingly, the current findings may suggest that the antiproliferative effect of **9e** *in vivo* was at least in part via enhancing necrosis of malignant cells.

*2.3.4. Effect of **9e** on JNK1 Gene and Protein Expression in Solid Tumors.* As shown in Figure 8A, **9e** at a dose of 30 mg/kg was capable of downregulating JNK1 gene expression by 47.3% when compared to the control untreated group. Comparatively, the SOR at 30 mg/kg was superior to **9e** at the two dose levels tested in reducing the gene expression of JNK1. On the other hand, protein levels of p-JNK were curtailed in

https://doi.org/10.1021/acsomega.4c05250
ACS Omega 2024, 9, 37310−37329

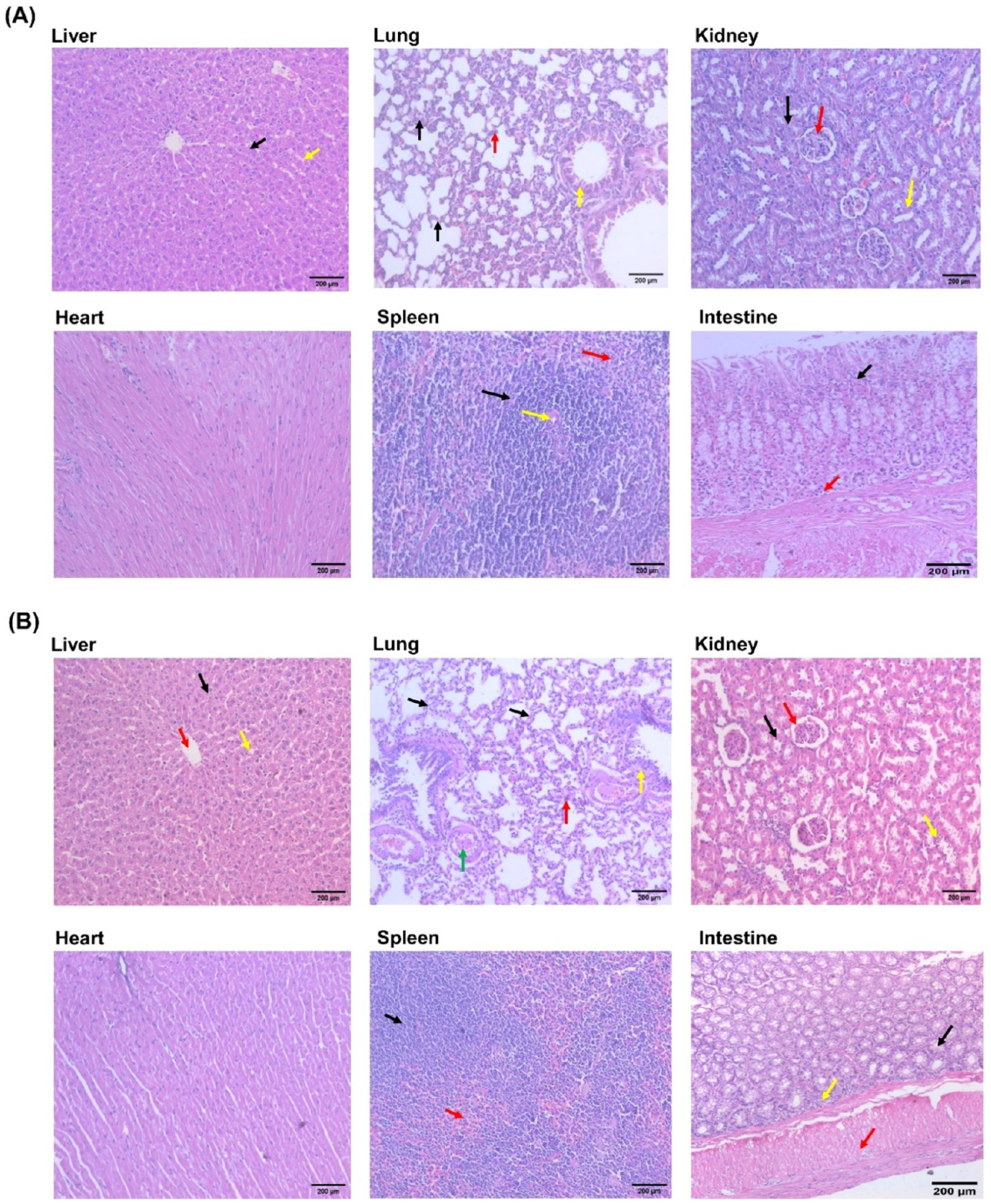

Figure 6. H&E-stained sections (×200) from the liver, lung, kidney, heart, spleen, and small intestine belonging to (A) normal and (B) 9e-treated groups. Liver sections from parts (A) and (B) show normal architecture, hepatocytes arranged in thin plates (black arrow), sinusoids (yellow arrow), and central veins (red arrow). Lung sections from parts (A) and (B) show normal alveoli with thin interalveolar septum (black arrow), type I and type II pneumocytes (red arrow), bronchus (yellow arrow), and blood vessels (green arrow). Kidney sections from parts (A) and (B) show normal renal cortex with normal renal corpuscle and glomerulus (red arrow), normal pattern of proximal convoluted (black arrow), and distal convoluted (yellow arrow) tubules. Heart sections from both groups show normal morphological appearance with normal myocardial muscle fibers. Spleen sections in both groups show a normal morphological appearance with normal white pulp (black arrow), red pulp (red arrow), and central arteriole (yellow arrow). Small intestine sections show normal mucosa lined by columnar mucin-secreting cells with normal villous pattern and goblet cells (black arrow), normal sub mucosa (yellow arrow), and muscle layer (red arrow).

SOR-, **9e** (15 mg/kg)-, and **9e** (30 mg/kg)-treated groups reaching 68.3, 52.5, and 67.7% reductions, respectively, relative to the control untreated group, where the differences were not significant between the treated groups (Figure 8B).

*2.3.5. Effect of **9e** on c-Jun and c-Fos Protein Levels in Solid Tumors.* To confirm JNK modulation by **9e**, levels of its downstream targets, c-Jun and c-Fos, were determined in tumor tissues. **9e** at 15 and 30 mg/kg dose levels elicited a 42 and 60% reduction in c-Jun levels in tumors compared to the control group, where the higher dose of **9e** achieved a comparable reduction to that of SOR (Figure 9A). Likewise, **9e** at 15 and 30 mg/kg caused 51.6 and 72.4% reduction in c-

https://doi.org/10.1021/acsomega.4c05250
ACS Omega 2024, 9, 37310−37329

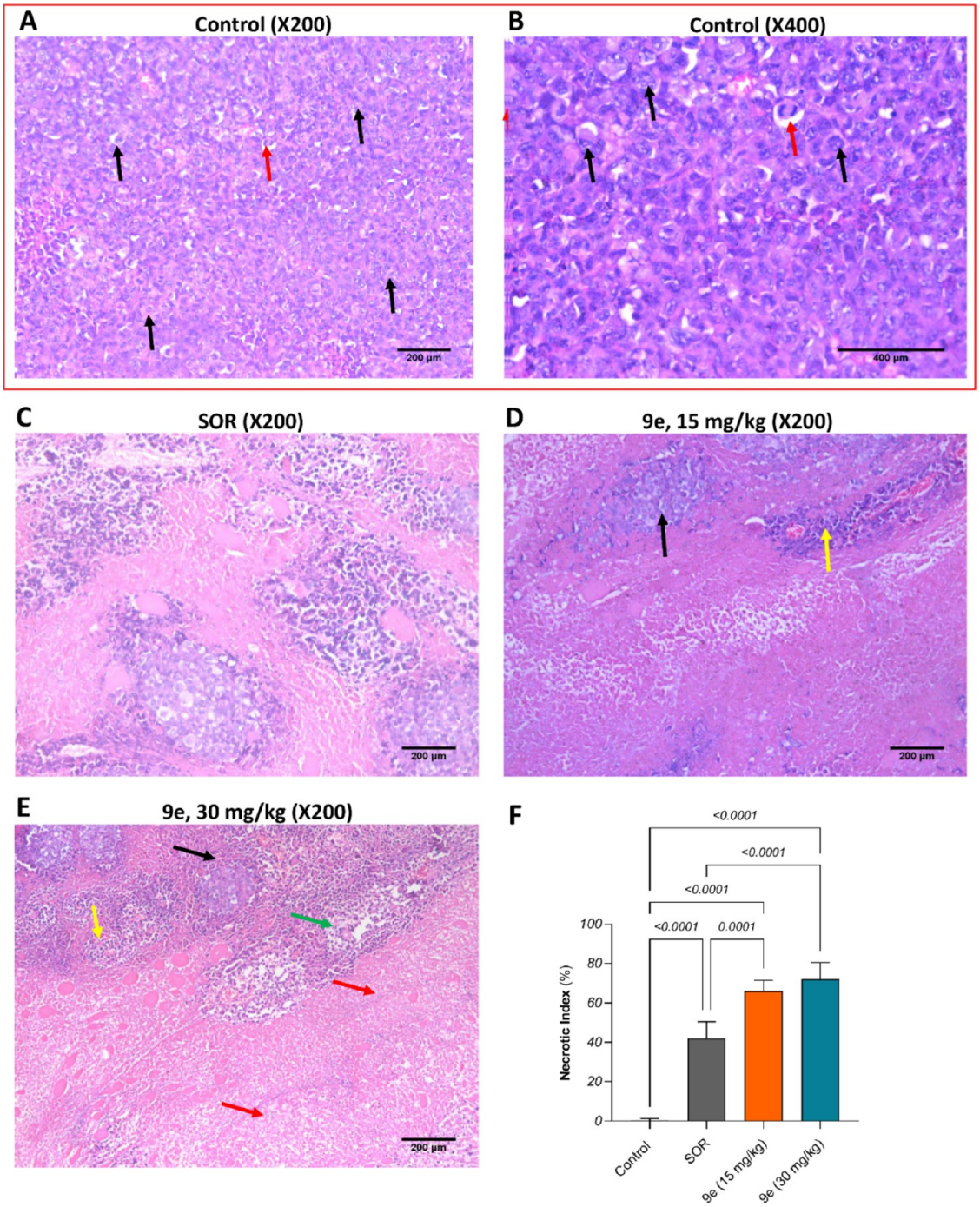

Figure 7. Effect of 9e on histopathological changes and necrotic indices. Photomicrographs of H&E-stained tumor sections from the control group at (A) ×200 and (B) ×400, (C) SOR-, (D) **9e** (15 mg/kg)-, and (E) **9e** (30 mg/kg)-treated groups. Black arrows indicate malignant cells; red arrows indicate increased cytoplasm-to-nucleus ratio in part (B) and areas of necrosis or apoptosis in parts (C-E); yellow arrows indicate apoptotic bodies; and green arrows indicate scattered macrophages. (F) Necrotic indices in control and treated groups. Values are presented as mean ± SD. One-way ANOVA followed by Tukey's post hoc test was applied for statistical analysis. P-values less than 0.05 were considered statistically significant.

Fos levels compared to the control untreated group, respectively, yet the effect of the higher dose of **9e** on c-Fos was commensurate to that of SOR (Figure 9B). These findings might imply that inhibition of c-Jun and c-Fos was downstream of JNK inhibition.

*2.3.6. Effect of **9e** on Cyclin D1 and p53 Gene Expression in Solid Tumors.* To investigate the effect of **9e**-mediated JNK inhibition on cell cycle progression, the gene expression of both cyclins D1 and p53 was sought. As demonstrated in Figure 9C, unlike SOR, neither a small dose nor a high dose of **9e** was capable of changing cyclin D1 gene expression levels relative to the positive control. P53, on the other hand, was upregulated by all treatments relative to the control group, where **9e** at low and high doses caused a 2- and a 3-fold increase in its gene expression levels, respectively (Figure 9D). These results may imply that the anticancer potential of **9e** is

https://doi.org/10.1021/acsomega.4c05250
ACS Omega 2024, 9, 37310−37329

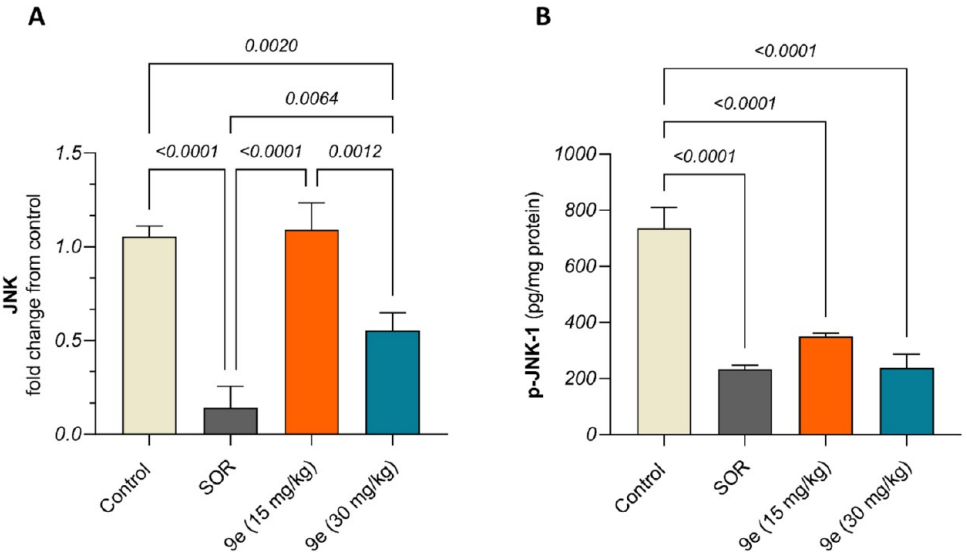

Figure 8. Effect of 9e on JNK gene expression and protein levels in solid tumors. (A) Gene expression analysis of JNK in solid tumors of the control and treated groups. (B) P-JNK protein levels in tumors of the control and treated groups. Relative gene expression (fold change from the control) was determined using qRT-PCR following normalization to the housekeeping GAPDH gene. Protein levels of p-JNK were estimated using ELISA. Values are presented as mean ± SD. One-way ANOVA followed by Tukey's post hoc test was applied for statistical analysis. P-values less than 0.05 were considered statistically significant.

due to the restoration of p53 activity rather than the inhibition of cyclin D1. The proposed anticancer mechanism of compound **9e** is illustrated in Figure 10.

In summary, the higher dose of **9e** (30 mg/kg) demonstrated enhanced effects on JNK gene expression, c-Fos, cyclin D1, and p53; however, it failed to alter other parameters such as tumor volume, necrotic index, JNK protein levels, and c-Jun, compared to the lower dose (15 mg/kg). These findings therefore highlight the inherent challenges in targeting JNK for inhibition. JNK inhibition is complicated by several factors intertwined with its interaction within particular cellular signaling pathways. The JNK family encompasses multiple isoforms, namely, JNK1, JNK2, and JNK3, each playing distinct roles across different tissues, which leads to variable efficacy and potential off-target effects depending on the targeted isoform. Additionally, JNK's involvement in apoptosis and cell survival introduces additional complexities, as prolonged inhibition can disrupt normal cellular functions and might promote resistance to apoptosis in tumor cells.[59] Moreover, the JNK pathways are altered by redundancy and compensatory mechanisms within the MAP kinase family; thus, inhibiting JNK may activate alternative pathways such as ERK or p38, diminishing the overall therapeutic impact.[60] Moreover, compensatory feedback regulation within the JNK signaling cascade adjusts the activity of both upstream and downstream components, adding layers of complexity to how cells respond to inhibition. On the other hand, JNK's crucial role in mediating inflammatory responses cannot be overlooked, as inhibiting JNK can alter immune function, leading to immunomodulatory effects that might be therapeutically undesirable in cancer contexts, especially at earlier stages.[61] These aforementioned aspects underscore the necessity for meticulous consideration of these dynamics in both the development and clinical applications of JNK inhibitors.

2.4. Molecular Docking. A molecular docking study was conducted to predict the binding mode of compound **9e** within the ATP binding pocket of human JNK1 (PDB ID: **4L7F**).[37] In this crystal structure, the cocrystallized ligand **AX13587** (PDB ID: **1 V5**) displayed the following key molecular interactions with the JNK1 binding pocket: dual hydrogen bonds with Met111 of the hinge region, a hydrogen bond with the catalytic Lys55, and another with the solvent-exposed Gln117.

FRED module of OpenEye software was used to simulate the docking experiment.[62−64]

First, docking validation for the software was performed by redocking the cocrystallized ligand **AX13587** in the binding site and evaluating the root-mean-square deviation (RMSD) between the cocrystallized and docked poses. The pose predicted by Fred showed a relatively high RMSD value of 2.739 Å with some deviation from the cocrystallized ligand and only reproduced one of the hydrogen bonds with Met111, one with Lys55, and another one with Asn114 instead of that with Gln117 (Figure 11B). Subsequently, the docking experiment was performed using AutoDock Vina.[65] Interestingly, AutoDock Vina succeeded in reproducing the same interactions of the cocrystallized ligand with an RMSD value of only 0.284 Å (Figure 11A). This finding gave AutoDock Vina better reliability in pose prediction of designed compound **9e** over FRED.

Since self-docking validation runs with RMSD between 2 and 3 Å may be considered acceptable,[66] the two docking programs were used to predict the binding mode of **9e**. As a result, two distinct binding modes of **9e** inside the binding pocket of JNK1 were obtained. The pose predicted by AutoDock Vina shows that the 3-methoxy group is pointing toward the hinge region, forming a hydrogen bond between the oxygen atom of the 3-methoxy group and the NH of Met111 amino acid, while the 4-methoxy group is pointing toward the solvent-exposed Gln117. On the other side, the 4-fluorophenyl group forms hydrophobic interactions with Glu73, Arg69, and Gln37 and occupies the aforementioned induced fit binding pocket formed by Glu73 and Arg69. The docking score of this pose was −9.4 kcal/mol, while that of the cocrystallized ligand is −11.2 kcal/mol. In comparison to the pose predicted by AutoDock Vina, the pose obtained from

https://doi.org/10.1021/acsomega.4c05250
ACS Omega 2024, 9, 37310−37329

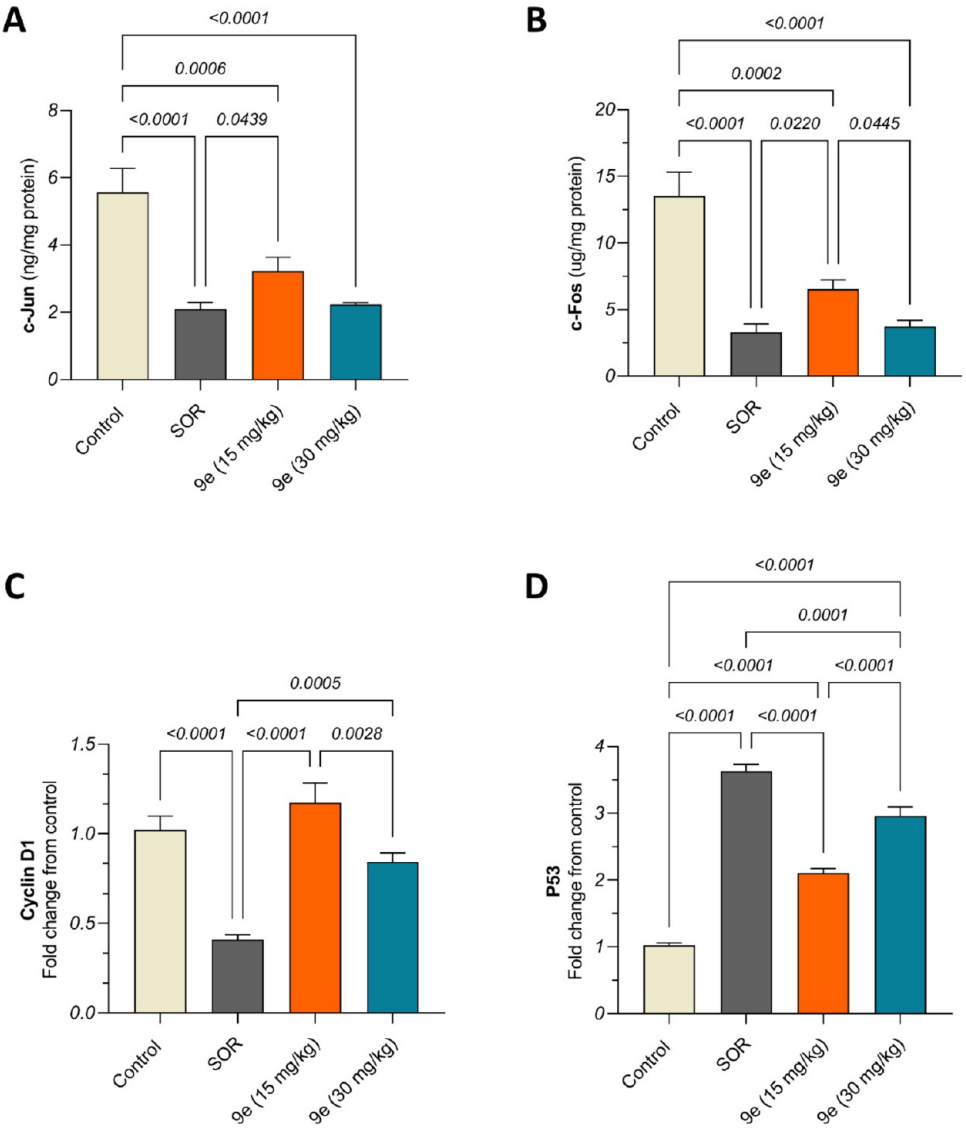

Figure 9. Effect of 9e on c-Jun and c-Fos protein levels as well as the gene expression of cyclin D1 and p53. (A) c-Jun and (B) c-Fos protein levels, as well as the gene expression analysis of (C) Cyclin D1 and (D) P53 in solid tumors of the control and treated groups. Protein levels of c-Jun and c-Fos were estimated using ELISA. Relative gene expression (fold change from the control) of cyclins D1 and P53 was determined using qRT-PCR following normalization to the housekeeping GAPDH gene. Values are presented as mean ± SD. One-way ANOVA followed by Tukey's post hoc test was applied for statistical analysis. *P*-values less than 0.05 were considered statistically significant.

FRED is flipped, where the 4-fluorophenyl group is directed toward the solvent-exposed Gln117. It shows a hydrogen bond between the oxygen atom of the carbonyl group and the NH of Met111 amino acid, with a docking score of −9.1 compared to −17.8, the docking score of the cocrystallized ligand. Figure 12 illustrates the 3D poses acquired from both docking experiments. Based on these results, the two distinct poses of docking of **9e** obtained from both software were subjected to molecular dynamics (MD) simulations.

2.5. Molecular Dynamics Simulations. Molecular dynamics (MD) simulations were performed to compare the stability of **9e** binding modes predicted by both docking programs, the FRED pose (referred herein as FRED) and AutoDock Vina pose (referred herein as Vina). **AX13587** was also subjected to MD simulations as a reference for pose and protein dynamics (referred to as the control), resulting in three MD runs. All MD runs were performed for 50 ns at the NPT ensemble for minimization and equilibration. For the three MD runs, the RMSD, a measure of structural stability over time, is calculated for the protein backbone atoms (Figure 13). After a very short time, the RMSD showed stability, with no significant fluctuations afterward across the three MD runs. The average RMSD was 1.85 ± 0.24, 2.00 ± 0.25, and 1.89 ± 0.39 Å (mean ± SD) for control, FRED, and Vina proteins, respectively. These findings indicate protein stability throughout the three production runs.

The root-mean-square fluctuation (RMSF) of protein residues revealed the protein's flexible sections. Generally, The RMSF graphs are overlapping, and most of the binding site residues have RMSF < 1.65 Å, indicating minimal local conformational changes in the binding site. As illustrated in Figure 14, the Vina complex showed three distinct flexible regions. The first region is depicted in Arg59 - Arg65, close to the binding site, with an average RMSF value of 2.30 Å. This movement might have been induced by ligand binding. However, the other fluctuating regions represented in

https://doi.org/10.1021/acsomega.4c05250
ACS Omega 2024, 9, 37310−37329

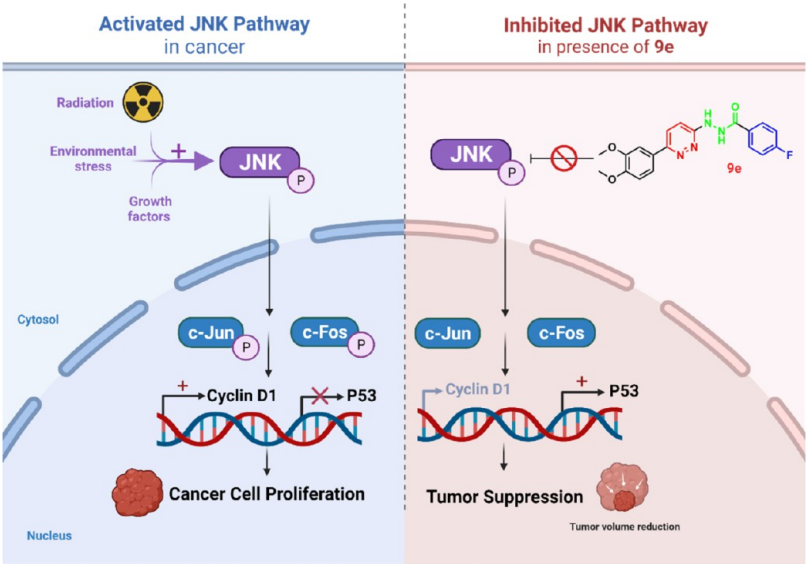

Figure 10. Schematic diagram illustrating the potential mechanism of action of 9e on the JNK pathway. Activation of the JNK pathway was previously reported to support cancer cell survival and proliferation. JNK phosphorylation leads to the activation of c-Jun and c-Fos, which consequently turn on the cell cycle by inducing the transcription of cyclin D1 and "break the brake" by suppressing P53. Our findings demonstrated a potential inhibitory effect of 9e on JNK along with its downstream targets, c-Jun and c-Fos, to enhance necrosis in tumors, likely via restoring p53 activity rather than curbing cyclin D1. ***Created with BioRender.com.***

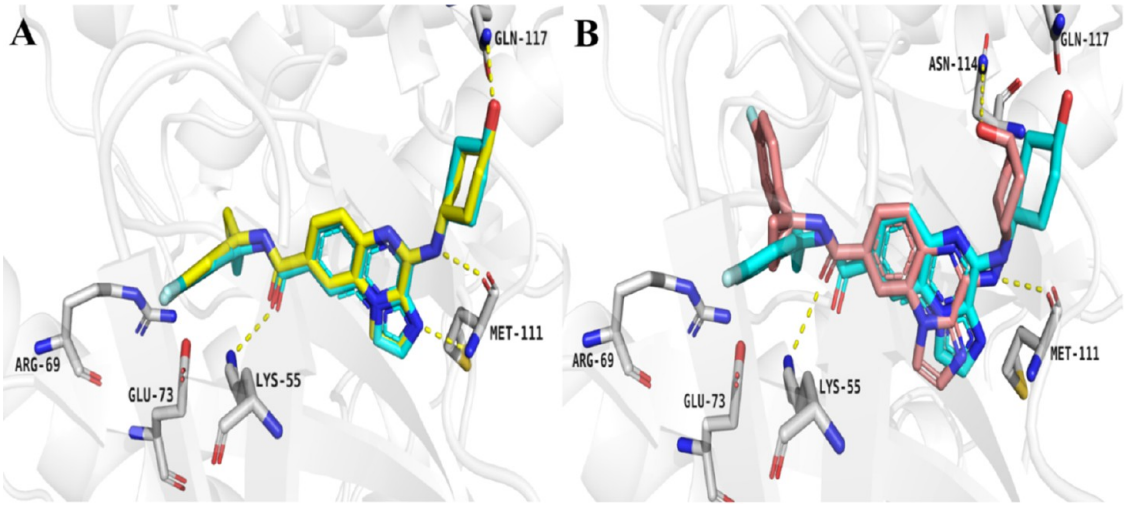

Figure 11. Results of docking validation. (A) AutoDock Vina predicted pose of AX13587 (yellow) is superimposed on the cocrystallized ligand AX13587 (cyan) with RMSD = 0.284 Å, while the pose predicted by FRED (pink) (B) shows some deviation with RMSD = 2.739 Å. Hydrogen bonds (yellow dashed lines) of the cocrystallized ligand with Met111 (bidentate), Lys55, and Gln117 are conserved by the AutoDock Vina docked pose, while the FRED docked pose reproduced only one of the hydrogen bonds with Met111, one with Lys55, and another one with Asn114 instead of that with Gln117.

Cys245 with an RMSF value of 2.19 Å and Asp326 - Pro334 with an average RMSF value of 2.52 Å are far from the binding site and not involved in the binding process. On the other hand, the FRED complex showed flexibility at the β sheet of Ile32 and Gly33 with an average RMSF value of 2.45 Å, which is also far from the binding site.

Additionally, protein conformation stability was also confirmed by the radius of gyration (R_g), a measure of the compactness of the protein structure. R_g values were found to be 22.41 ± 0.13, 22.42 ± 0.12, and 22.27 ± 0.24 nm (mean ± SD) for control, FRED, and Vina proteins, respectively (Figure 15). R_g values revealed that the Vina mode of **9e** shows a lower R_g than the control and FRED modes, indicating more compactness and hence stability.

Furthermore, ligand RMSD analysis (Figure 16) assessed for the three MD runs demonstrated that **AX13587** had the least deviation with an RMSD value of 0.89 ± 0.24 Å (mean ± SD). On comparing the RMSD of both binding modes of **9e**, the FRED binding mode significantly revealed a greater deviation with an average RMSD value of 7.60 ± 1.48, while that of the Vina binding mode was 2.29 ± 0.18 Å (mean ± SD). This suggests that the FRED binding mode of **9e** has been moved from its initial pose. Careful investigation of the trajectories revealed that after about 10 ns, the FRED binding mode of **9e** started to abandon its initial place and moved outside the binding site (Figure 17). Conversely, the lower RMSD of the Vina binding mode for **9e** confirmed its stability. Detailed analysis of the Vina binding mode throughout all of the

https://doi.org/10.1021/acsomega.4c05250
ACS Omega 2024, 9, 37310−37329

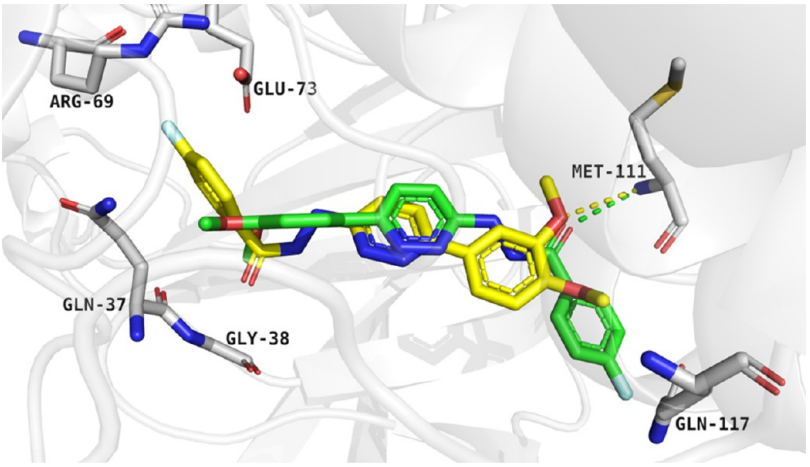

Figure 12. Binding mode of **9e** predicted by AutoDock Vina (yellow), showing one hydrogen bond with Met111 (yellow dashed line). In addition, the 4-fluorophenyl group occupies the induced fit binding pocket formed by Glu73 and Arg69. While the flipped pose of FRED (green) shows one hydrogen bond with Met111 (green dashed lines), the 4-fluorophenyl group is directed toward the solvent-exposed Gln117.

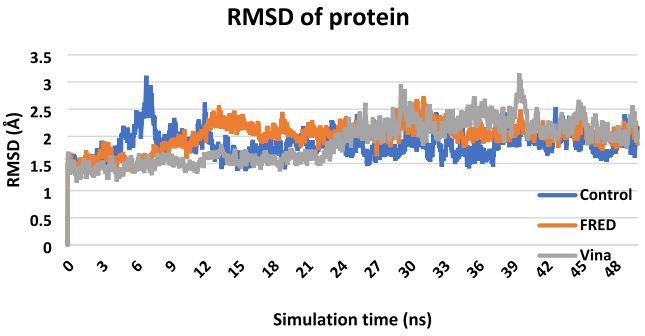

Figure 13. Protein RMSD of the three MD runs.

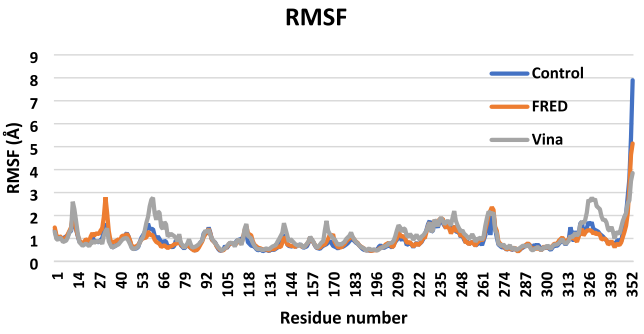

Figure 14. Per residue RMSF of the studied complexes throughout the MD runs.

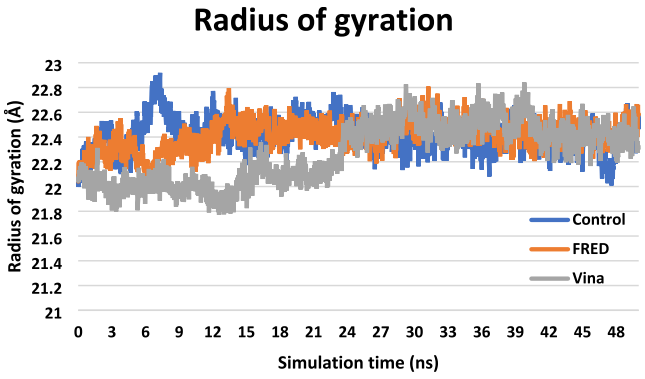

Figure 15. Protein radius of gyration (R_g) of the three MD runs.

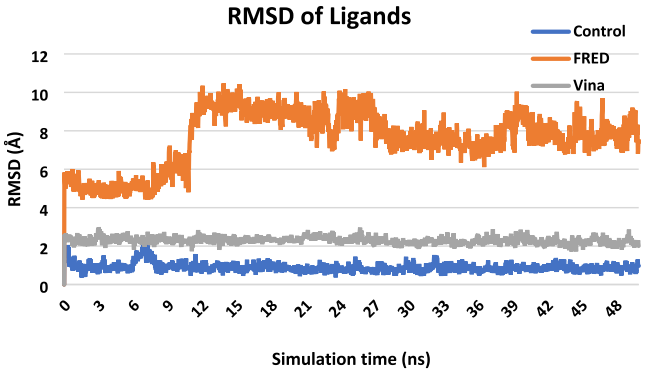

Figure 16. RMSD of heavy ligand heavy atoms.

trajectories showed that at the very first nanoseconds, the 4-fluorophenyl group has slightly moved to adopt almost the same orientation as the cocrystallized ligand (Figure 18). Finally, the effect of hydrogen bonding on the overall binding interactions was investigated between the ligands and their proteins (Figure 19). **AX13587**, FRED, and Vina had 1.07 ± 1.12, 0.60 ± 0.95, and 1.20 ± 0.78 (mean ± SD) hydrogen bonds through the 50 ns simulation time. The higher average number of hydrogen bonds of Vina mode compared to the number of hydrogen bonds of **AX13587** and FRED mode indicates its binding stability. In conclusion, from the results obtained from the docking studies together with comparing the number of hydrogen bonds during the entire MD simulation and RMSD of both docked poses, the Vina binding mode is suggested to be the binding mode adopted by **9e** inside the JNK1 protein. Furthermore, it correlates with the results of the *in vitro* antiproliferative screening studies, where all of the derivatives lacking either the 3-methoxy or the 4-fluorophenyl groups are relatively less active.

3. CONCLUSIONS

Novel 3,6-disubstituted pyridazine derivatives were designed and synthesized. Subsequently, the NCI-60 cancer cell line screening of the 15 synthesized compounds identified the broad-spectrum antiproliferative activity of compound **9e** with the highest inhibitory activity on renal and breast cancer cell

https://doi.org/10.1021/acsomega.4c05250
ACS Omega 2024, 9, 37310−37329

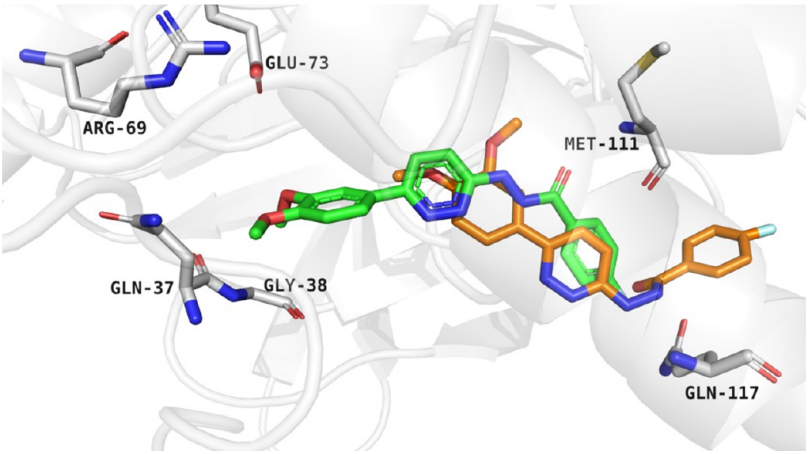

Figure 17. Comparing the FRED binding mode of **9e** in the first frame of the MD simulation (green) and the last frame (orange) showing its movement outside the binding site.

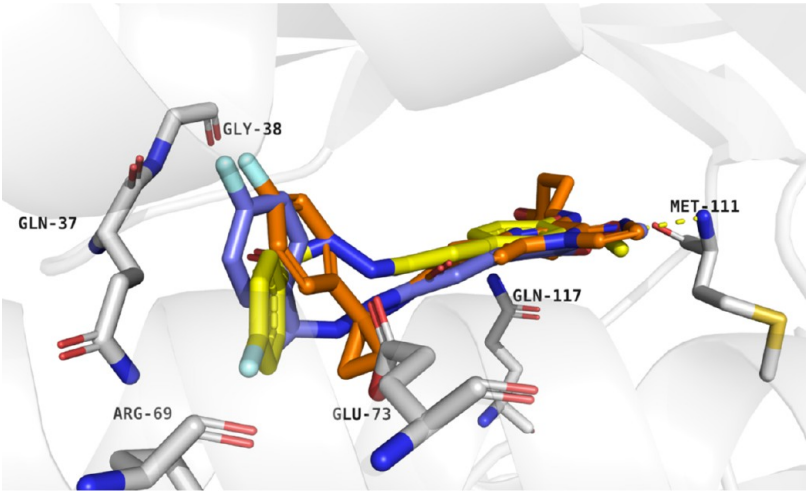

Figure 18. Comparing the Vina binding mode of **9e** at the first frame of the MD simulation (yellow) and the last frame (purple) with the binding mode of the cocrystallized ligand (orange).

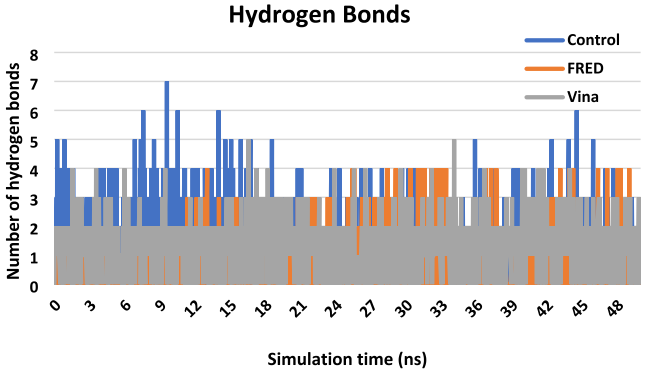

Figure 19. Number of hydrogen bonds between the ligands and protein during the MD production runs.

lines, where it demonstrated 97.91 and 79.98% inhibition on A498 renal cancer cell line and T-47D breast cancer cell line, respectively. Furthermore, the NCI five-dose testing of compound **9e** revealed the most potent antiproliferative activity against the NSCLC subpanel, with a GI_{50} value of 17.8 μM on the HOP-92 cell line, followed by the breast, CNS, renal, and leukemia cancer subpanels.

The *in vivo* anticancer activity of **9e** was then evaluated, demonstrating tumor volume regression and enhanced necrosis. Additionally, a potential inhibitory effect on JNK1 and its downstream targets, c-Jun and c-Fos, was evident, mirroring an upregulation in p53 in solid tumors. Molecular docking and dynamics simulations have proposed the binding mode of **9e** inside the JNK1 binding pocket and confirmed its stability in the binding site. These findings imply that our best hit **9e** could be a promising scaffold to probe JNK1 as a molecular target for the development of novel anticancer agents. Further investigation into compounds featuring the p-fluorophenyl moiety for JNK inhibition is recommended. Furthermore, benchmarking the current findings against established JNK inhibitors, such as SP600125, would provide a more robust validation of the results and enhance the comparative understanding of efficacy.

4. EXPERIMENTAL SECTION

4.1. Chemistry. Melting points were measured with a Stuart SMP 30 apparatus and were uncorrected. IR spectra were recorded on a Shimadzu FT-IR 8400S infrared spectrophotometer. ^{1}H NMR spectra were run at 400 MHz, and ^{13}C NMR spectra were run at 100 MHz in deuterated

https://doi.org/10.1021/acsomega.4c05250
ACS Omega 2024, 9, 37310−37329

dimethyl sulfoxide (DMSO-d_6) on a Bruker Ascend 400/R instrument at the Microanalytical Unit, Faculty of Pharmacy, Cairo University. Chemical shifts (δ) were reported relative to TMS as an internal standard (Figures S1−S34). All coupling constant (J) values are given in Hz. Elemental analyses performed on a Thermo Scientific Flash 2000 elemental Analyzer and mass spectrometry recorded on a Thermo Scientific GCMS model ISQ mass spectrometer were carried out at the Regional Center for Mycology and Biotechnology, Al-Azhar University, Cairo, Egypt. Thin layer chromatography (TLC) carried out on silica gel plates purchased from Merck was employed routinely to follow the course of reactions and to check the purity of products. All reagents and solvents were purified and dried by standard techniques. Compounds **3a**,[38] **4a**,[39] and **5a**[40] were synthesized according to the reported procedures.

*4.1.1. Procedure for Preparation of 6-(3,4-Dimethoxyphenyl)pyridazin-3(2H)-one (**3b**).* A mixture of 3′,4′-dimethoxyacetophenone (**2b**) (1.0 mmol, 2.16g), glyoxylic acid monohydrate (**1**) (1.3 mmol, 1.15g), and acetic acid (24 mL) was refluxed for 10 h. After that, the reaction mixture was cooled in an ice bath, and 60 mL of water and aqueous ammonia (25%) were added until the medium pH became 8. Then, the reaction mixture was extracted with methylene chloride (3 × 25 mL). To the ammoniacal solution, hydrazine hydrate (99%, 10 mmol, 6 mL) was added, and the reaction mixture was heated under reflux for 2 h. After completion, the reaction mixture was cooled down. The obtained precipitate was filtered, washed with water, and used without further purification. Yield: 93% (0.213 g), m.p.= 219−221 °C. **IR (KBr disk) (cm^{-1}):** 3201 (NH), 3012−2962 (CH aromatic), 2931−2835 (CH aliphatic), 1678 (C═O), 1600 (C═N), 1581 (C═C). **^{1}H NMR (400 MHz, DMSO-d_6):** δ 13.00 (s, 1H, NH), 8.02 (d, J = 10 Hz, 1H, H pyridazinone), 7.41−7.39 (m, 2H, Ar−H), 7.02 (d, J = 8.2 Hz, 1H, Ar−H), 6.96 (d, J = 10 Hz, 1H, H pyridazinone), 3.82 (s, 3H, OCH_3), 3.78 (s, 3H, OCH_3). **MS:** m/z (%) 232.87 (M^+, 63), 109 (100). **Anal. Calcd** for $C_{12}H_{12}N_2O_3$ (232.24): C, 62.06; H, 5.21; N, 12.06 Found: C, 61.87; H, 5.43; N, 12.3.

*4.1.2. Procedure for Preparation of 3-Chloro-6-(3,4-dimethoxyphenyl)pyridazine (**4b**).* A mixture of the appropriate pyridazinone **3b** (0.0175 mol, 4.06g) and phosphorus oxychloride (17 mL, 0.182 mol) was refluxed at 100 °C for 2 h. After it was cooled, the reaction mixture was poured on ice (20 mL), and its pH was brought to 7 by sodium carbonate. The formed precipitate was filtered, washed with water, and dried under reduced pressure. Yield: 94% (4.1 g), mp 155 °C. **^{1}H NMR (400 MHz, DMSO-d_6):** δ 8.32 (d, J = 9.0 Hz, 1H, H pyridazine), 7.94 (d, J = 9.0 Hz, 1H, H pyridazine), 7.75−7.71 (m, 2H, Ar−H), 7.12 (d, J = 8.4 Hz, 1H, Ar−H), 3.87 (s, 3H, OCH_3), 3.84 (s, 3H, OCH_3). **^{13}C NMR (100 MHz, DMSO):** δ 158.30, 155.03, 151.40, 149.57, 129.52, 127.48, 120.57, 112.33, 110.20 (Ar−C), 56.06, 56.04 (OCH_3). **Anal. Calcd** for $C_{12}H_{11}ClN_2O_2$ (250.68): C, 57.50; H, 4.42; Cl, 14.14; N, 11.18 Found: C, 57.47; H, 4.59; N, 11.41.

*4.1.3. Procedure for Preparation of 6-(3,4-Dimethoxyphenyl)pyridazin-3-yl Hydrazine (**5b**).* A mixture of 3-chloro-6-(3,4-dimethoxyphenyl)pyridazine (**4b**) (52.5 mmol, 13.16g) and hydrazine hydrate (99%, 51.4 mL, 1049 mmol) was stirred at 130 °C for 1 h. The reaction mixture was cooled and then concentrated under reduced pressure. The resultant product was filtered, washed with plenty of water, dried, and then crystallized from isopropanol. Yield: 97% (12.5 g), mp 95−100 °C. **IR (KBr disk) (cm^{-1}):** 3560−3259 (NH, NH_2), 3093−3012 (CH aromatic), 2939−2843 (CH aliphatic), 1604 (C═N), 1512 (C═C). **^{1}H NMR (400 MHz, DMSO-d_6):** δ 7.96 (s, 1H, NH, D_2O exchangeable), 7.86 (d, J = 9.4 Hz, 1H, H pyridazine), 7.63 (d, J = 2.1 Hz, 1H, Ar−H), 7.49 (dd, J = 8.3, 2.1 Hz, 1H, Ar−H), 7.09 (d, J = 9.4 Hz, 1H, H pyridazine), 7.03 (d, J = 8.4 Hz, 1H, Ar−H), 4.35 (br s, 2H, NH_2, D_2O exchangeable), 3.84 (s, 3H, OCH_3), 3.80 (s, 3H, OCH_3). **MS:** m/z (%) 246 (M^+, 100). **Anal. Calcd** for $C_{12}H_{14}N_4O_2$ (246.27): C, 58.53; H, 5.73; N, 22.75. Found: C, 58.76; H, 5.86; N, 22.98.

*4.1.4. Procedure for Preparation of N′-(6-phenylpyridazin-3-yl)-4-toluenesulfonohydrazide (**7**).* Compound **5a** (0.558 g, 3 mmol) was dissolved in dry methylene chloride (5 mL), and then triethylamine (0.5 mL) was added at room temperature. After cooling the solution to 0 °C, 4-toluenesulfonyl chloride (0.572 g, 3 mmol) was then added dropwise. The reaction mixture was allowed to come to RT, stirred for 3 h, dried under reduced pressure, and then the residue was crystallized from ethanol. Yield: 62% (0.63 g), mp 212−215 °C. **IR (KBr disk) (cm^{-1}):** 3213−3136 (NH, NH), 3059(CH aromatic), 2958−2924 (CH aliphatic), 1608 (C═N), 1550 (C═C aromatic), 1446, 1415 (forked peak) and 1165 (SO_2). **^{1}H NMR (400 MHz, DMSO-d_6):** δ 9.92 (s, 1H, NH−SO_2, D_2O exchangeable), 9.17 (s, 1H, NH, D_2O exchangeable), 7.99−7.96 (m, 3H, Ar−H + H pyridazine), 7.76 (d, J = 8.2 Hz, 2H, Ar−H), 7.49 (t, J = 8.2 Hz, 2H, Ar−H), 7.44 (d, J = 8.0 Hz, 1H, Ar−H), 7.40 (d, J = 8.8 Hz, 2H, Ar−H), 7.19 (d, J = 9.4 Hz, 1H, H pyridazine), 2.38 (s, 3H, CH_3). **^{13}C NMR (100 MHz, DMSO):** δ 161.05, 152.84, 143.96, 136.94, 136.06, 130.04, 129.3, 129.29, 128.23, 126.25, 113.46(Ar−C), 21.50(CH_3). **MS:** m/z (%) 340 (M^+, 23), 156 (100). **Anal. Calcd** for $C_{17}H_{16}N_4O_2S$ (340.40): C, 59.98; H, 4.74; N, 16.46; S, 9.42. Found: C, 60.12; H, 4.86; N, 16.63; S, 9.58.

*4.1.5. General Procedure for Preparation of N′-(6-substituted phenylpyridazin-3-yl)-4-substituted Benzenecarbohydrazides (**9a−g**).* To a stirred solution at 0 °C of the appropriate 6-substituted phenylpyridazin-3-yl hydrazine (**5a−b**) (7.14 mmol) in diethyl ether (29 mL) and triethylamine (1.0 mL, 0.72 g, 7.14 mmol), substituted benzoyl chloride (**8a−d**) (7.14 mmol) was added dropwise. After stirring at RT for 1 h, the formed precipitate was filtered, washed with water and then hexane, and finally with ethanol, and dried under reduced pressure to provide the corresponding hydrazides **9a−g**.

*4.1.5.1. N′-(6-Phenylpyridazin-3-yl)benzohydrazide (**9a**).* Yield: 83% (1.716 g), mp 202−205 °C. **IR (KBr disk) (cm^{-1}):** 3255−3170 (NH, NH), 3047 (CH aromatic), 1651 (C═O), 1600 (C═N), 1577 (C═C aromatic). **^{1}H NMR (400 MHz, DMSO-d_6):** δ 10.64 (s, 1H, NH-C═O, D_2O exchangeable), 9.18 (s, 1H, NH, D_2O exchangeable), 8.03−7.96 (m, 5H, Ar−H+ H pyridazine), 7.63−7.41 (m, 6H, Ar−H), 7.09 (d, J = 9.3 Hz, 1H, H pyridazine). **^{13}C NMR (100 MHz, DMSO):** δ 166.87 (C═O), 160.53, 152.69, 137.12, 133.09, 132.35, 129.30, 129.21, 128.98, 127.97, 126.27, 126.22, 113.68 (Ar−C). **MS:** m/z (%) 290 (M^+, 12), 105 (100). **Anal. Calcd** for $C_{17}H_{14}N_4O$ (290.33): C, 70.33; H, 4.86; N, 19.30. Found: C, 70.61; H, 5.67; N, 19.52.

*4.1.5.2. 4-Methoxy-N′-(6-phenylpyridazin-3-yl)-benzohydrazide (**9b**).* Yield: 90% (2.06 g), mp 219−220 °C. **IR (KBr disk) (cm^{-1}):** 3302−3248 (NH, NH), 3062−3005 (CH aromatic), 2912−2839 (CH aliphatic), 1681 (C═O),

https://doi.org/10.1021/acsomega.4c05250
ACS Omega 2024, 9, 37310−37329

1647 (C═N), 1577 (C═C aromatic). **^{1}H NMR (400 MHz, DMSO-d_6):** δ 10.47 (s, 1H, NH-C═O, D_2O exchangeable), 9.08 (s, 1H, NH, D_2O exchangeable), 8.02−7.94 (m, 5H, Ar−H+ H pyridazine), 7.52−7.41 (m, 3H, Ar−H), 7.06 (m, 3H, Ar−H+ H pyridazine), 3.84 (s, 3H, OCH_3). **^{13}C NMR (100 MHz, DMSO):** δ 166.45 (C═O), 162.54, 160.68, 152.65, 137.09, 129.86, 129.31, 129.21, 126.28, 126.20, 125.16, 114.22, 113.66 (Ar−C), 55.88 (OCH_3). **MS:** *m*/*z* (%) 320 (M^+, 36), 258 (100). **Anal. Calcd** for $C_{18}H_{16}N_4O_2$ (320.35): C, 67.49; H, 5.03; N, 17.49. Found: C, 67.70; H, 5.14; N, 17.63.

*4.1.5.3. 4-Fluoro-N′-(6-phenylpyridazin-3-yl)-benzohydrazide (**9c**).* Yield: 93% (2.05 g), mp 217−219 °C. **IR (KBr disk) (cm^{-1}):** 3506, 3410 (NH, NH), 3062 (CH aromatic), 1666 (C═O), 1635 (C═N), 1593 (C═C aromatic). **^{1}H NMR (400 MHz, DMSO-d_6):** δ 10.65 (s, 1H, NH-C═O, D_2O exchangeable), 9.16 (s, 1H, NH, D_2O exchangeable), 8.06−7.96 (m, 5H, Ar−H + H pyridazine), 7.52−7.36 (m, 5H, Ar−H), 7.09 (d, *J* = 9.3 Hz, 1H, H pyridazine). **MS:** *m*/*z* (%) 309 (M^+, 11), 123 (100). **Anal. Calcd** for $C_{17}H_{13}FN_4O$ (308.32): C, 66.23; H, 4.25; N, 18.17. Found: C, 66.40; H, 4.17; N, 18.29.

*4.1.5.4. N′-(6-(3,4-Dimethoxyphenyl)pyridazin-3-yl)-benzohydrazide (**9d**).* Yield: 53% (1.33 g), mp 196−198 °C. **IR (KBr disk) (cm^{-1}):** 3255−3140 (NH, NH), 3082−3055 (CH aromatic), 2962−2835 (CH aliphatic), 1666 (C═O), 1604 (C═N), 1519 (C═C aromatic). **^{1}H NMR (400 MHz, DMSO-d_6):** δ 10.58 (s, 1H, NH-C═O, D_2O exchangeable), 9.04 (s, 1H, NH, D_2O exchangeable), 7.97−7.95 (m, 3H, Ar−H + H pyridazine), 7.65 (d, *J* = 2.1 Hz, 1H, Ar−H), 7.61 (t, *J* = 7.2 Hz, 1H, Ar−H), 7.56−7.52 (m, 3H, Ar−H), 7.07−7.03 (m, 2H, Ar−H + H pyridazine), 3.84 (s, 3H, OCH_3), 3.81 (s, 3H, OCH_3). **^{13}C NMR (100 MHz, DMSO):** δ 166.90 (C═O), 160.10, 152.50, 150.07, 149.50, 133.11, 132.33, 129.75, 128.98, 127.93, 125.89, 118.78, 113.85, 112.31, 109.52 (Ar−C), 56.02, 55.95 (OCH_3). **MS:** *m*/*z* (%) 350 (M^+, 17), 332 (100). **Anal. Calcd** for $C_{19}H_{18}N_4O_3$ (350.38): C, 65.13; H, 5.18; N, 15.99. Found: C, 65.07; H, 5.47; N, 16.23.

*4.1.5.5. N′-(6-(3,4-Dimethoxyphenyl)pyridazin-3-yl)-4-fluorobenzohydrazide (**9e**).* Yield: 69% (1.81 g), mp 186−188 °C. **IR (KBr disk) (cm^{-1}):** 3286-3140 (NH, NH), 3074−3008 (CH aromatic), 2951−2835 (CH aliphatic), 1674 (C═O), 1651 (C═N), 1504 (C═C aromatic). **^{1}H NMR (400 MHz, DMSO-d_6):** δ 10.63 (s, 1H, NH-C═O, D_2O exchangeable), 9.07 (s, 1H, NH, D_2O exchangeable), 8.04 (dd, *J* = 8.5, 5.5 Hz, 2H, Ar−H), 7.95 (d, *J* = 9.3 Hz, 1H, H pyridazine), 7.66 (d, *J* = 2.0 Hz, 1H, Ar−H), 7.52 (dd, *J* = 8.4, 2.0 Hz, 1H, Ar−H), 7.38 (t, *J* = 8.7 Hz, 2H, Ar−H), 7.06 (m, 2H, Ar−H + H pyridazine), 3.84 (s, 3H, OCH_3), 3.81 (s, 3H, OCH_3). **^{13}C NMR (100 MHz, DMSO):** δ 165.86 (C═O), 163.46, 160.03, 152.55, 150.09, 149.50, 130.71, 130.62, 129.75, 129.62, 129.59, 125.88, 118.78, 116.07, 115.86, 113.92, 112.28, 109.53, (Ar−C), 56.00, 55.94 (OCH_3). **MS:** *m*/*z* (%) 368 (M^+, 26), 123 (100). **Anal. Calcd** for $C_{19}H_{17}FN_4O_3$ (368.37): C, 61.95; H, 4.65; N, 15.21. Found: C, 62.18; H, 4.88; N, 15.47.

*4.1.5.6. N′-(6-(3,4-Dimethoxyphenyl)pyridazin-3-yl)-4-methoxybenzohydrazide (**9f**).* Yield: 68% (1.85 g), mp 185−189 °C. **IR (KBr disk) (cm^{-1}):** 3506−3332 (NH, NH), 3070−3001 (CH aromatic), 2962−2839 (CH aliphatic), 1654 (C═O), 1604 (C═N), 1469 (C═C aromatic). **^{1}H NMR (400 MHz, DMSO-d_6):** δ 10.43 (s, 1H, NH-C═O, D_2O exchangeable), 8.98 (s, 1H, NH, D_2O exchangeable), 7.95−7.93 (m, 3H, Ar−H + H pyridazine), 7.65 (d, *J* = 2.0 Hz, 1H, Ar−H), 7.52 (dd, *J* = 8.4, 2.1 Hz, 1H, Ar−H), 7.08−7.05 (m, 3H, Ar−H), 7.02 (d, *J* = 9.5 Hz, 1H, H pyridazine), 3.84 (s, 3H, OCH_3), 3.82 (s, 3H, OCH_3), 3.81 (s, 3H, OCH_3). **^{13}C NMR (100 MHz, DMSO):** δ 166.53 (C═O), 162.52, 160.24, 152.48, 150.04, 149.46, 129.84, 129.70, 125.94, 125.16, 118.80, 114.21, 113.87, 112.28, 109.46(Ar−C), 56.00, 55.93, 55.87 (OCH_3). **MS:** *m*/*z* (%) 381 (M^+, 11), 44 (100). **Anal. Calcd** for $C_{20}H_{20}N_4O_4$ (380.40): C, 63.15; H, 5.30; N, 14.73. Found: C, 63.42; H, 5.47; N, 14.91.

*4.1.5.7. 4-Bromo-N′-(6-(3,4-dimethoxyphenyl)pyridazin-3-yl)benzohydrazide (**9g**).* Yield: 81% (2.49 g), mp 168−170 °C. **IR (KBr disk) (cm^{-1}):** 3271, 3213 (NH, NH), 3070−2958 (CH aromatic), 2935−2835 (CH aliphatic), 1674 (C═O), 1589 (C═N), 1519 (C═C aromatic). **^{1}H NMR (400 MHz, DMSO-*d6*):** δ 10.67 (s, 1H, NH-C═O, D_2O exchangeable), 9.07 (s, 1H, NH, D_2O exchangeable), 7.94 (d, *J* = 9.4, 1H, H pyridazine), 7.89 (d, *J* = 8.4, 2H, Ar−H), 7.74 (d, *J* = 8.4, 2H, Ar−H), 7.65 (d, *J* = 1.6 Hz, 1H, Ar−H), 7.52 (dd, *J* = 8.5, 1.7 Hz, 1H, Ar−H), 7.05−7.07 (m, 2H, Ar−H + H pyridazine), 3.84 (s, 3H, OCH_3), 3.81 (s, 3H, OCH_3). **^{13}C NMR (100 MHz, DMSO):** δ 166.21(C═O), 159.83, 152.63, 150.07, 149.45, 132.18, 132.15, 132.05, 131.76, 130.03, 129.61, 126.14, 126.00, 118.85, 114.09, 112.27, 109.47 (Ar−C), 56.00, 55.93 (OCH_3). **MS:** *m*/*z* (%) 429 (M^+, 11), 245 (100). **Anal. Calcd** for $C_{19}H_{17}BrN_4O_3$ (429.27): C, 53.16; H, 3.99; N, 13.05. Found: C, 53.43; H, 4.15; N, 13.21.

*4.1.6. General Procedure for Preparation of N-(substituted phenyl)- 2-(6-substituted phenylpyridazin-3-yl)-hydrazine-1-carboxamides (**11a, c, e**) and N-substituted phenyl-2-(6- substituted phenylpyridazin-3-yl)hydrazine-1-carbothioamides (**11b, d, f, g**).* To a mixture of the appropriate 3-hydrazinylpyridazines (**5**) (1.65 mmol) and triethylamine (0.25 mL) in dry methylene chloride (5 mL) at 0 °C, the appropriate phenyl isocyanate or phenyl isothiocyanate (**10a-d**) (1.65 mmol) was added dropwise. The reaction was stirred at RT for 6 h, and the obtained precipitate was filtered off and then washed with ethanol. All compounds were purified by column chromatography.

*4.1.6.1. N-(4-Chlorophenyl)-2-(6-phenylpyridazin-3-yl)-hydrazine-1-carboxamide (**11a**).* Yield: 76% (0.42 g), mp 217−219 °C. **IR (KBr disk) (cm^{-1}):** 3221−3113 (NH, NH, NH), 3051 (CH aromatic), 1666 (C═O), 1593 (C═N), 1535 (C═C aromatic). **^{1}H NMR (400 MHz, DMSO-d_6):** δ 9.10 (s, 1H, NH-C═O, D_2O exchangeable), 8.93 (s, 1H, NH-C═O, D_2O exchangeable), 8.43 (s, 1H, NH, D_2O exchangeable), 8.02−7.98 (m, 3H, Ar−H+ H pyridazine), 7.58 (d, *J* = 8.4 Hz, 2H, Ar−H), 7.50 (t, *J* = 7.4 Hz, 2H, Ar−H), 7.44 (d, *J* = 7.2 Hz, 1H, Ar−H), 7.30 (d, *J* = 8.9 Hz, 2H, Ar−H), 7.09 (d, *J* = 9.3 Hz, 1H, H pyridazine). **^{13}C NMR (100 MHz, DMSO):** δ 160.79(C═O), 156.67, 152.84, 139.25, 137.11, 129.31, 129.23, 128.85, 126.25, 126.23, 125.90, 120.71, 113.87(Ar−C). **MS:** *m*/*z* (%) 339 (M^+, 10), 186 (100). **Anal. Calcd** for $C_{17}H_{14}ClN_5O$ (339.78): C, 60.09; H, 4.15; N, 20.61. Found: C, 60.27; H, 4.34; N, 20.89.

*4.1.6.2. N-Phenyl-2-(6-phenylpyridazin-3-yl)hydrazine-1-carbothioamide (**11b**).* Yield: 65% (0.33 g), mp 174−176 °C. **IR (KBr disk) (cm^{-1}):** 3321−3151 (NH, NH, NH), 3016 (CH aromatic), 1597 (C═N), 1535 (C═C aromatic), 1219 (C═S). **^{1}H NMR (400 MHz, DMSO-d_6):** δ 10.01 (s, 1H, NH-C═S, D_2O exchangeable), 9.88 (s, 1H, NH-C═S, D_2O exchangeable), 9.25 (s, 1H, NH, D_2O exchangeable), 8.08−8.03 (m, 3H, Ar−H + H pyridazine), 7.56−7.45 (m, 5H, Ar−H), 7.32 (t, *J* = 7.7 Hz, 2H, Ar−H), 7.14 (t, *J* = 7.3 Hz, 1H,

https://doi.org/10.1021/acsomega.4c05250
ACS Omega 2024, 9, 37310−37329

Ar−H), 7.04 (d, J = 9.3 Hz, 1H, H pyridazine). **^{13}C NMR (100 MHz, DMSO):** δ 181.97 (C═S), 160.15, 153.37, 139.66, 136.98, 129.40, 129.37, 128.40, 126.41, 126.31, 125.92, 125.36, 114.18 (Ar−C). **MS:** m/z (%) 322 (M^+, 16), 57 (100). **Anal. Calcd** for $C_{17}H_{15}N_5S$ (321.40): C, 63.53; H, 4.70; N, 21.79; S, 9.98. Found: C, 63.79; H, 4.63; N, 22.05; S, 10.14.

*4.1.6.3. N-(4-Methoxyphenyl)-2-(6-phenylpyridazin-3-yl)-hydrazine-1-carboxamide (**11c**).* Yield: 77% (0.42 g), mp 211−213 °C. **IR (KBr disk) (cm^{-1}):** 3329, 3248, 3232 (NH, NH, NH), 3062−3008 (CH aromatic), 2958−2935 (CH aliphatic), 1658 (C═O), 1597 (C═N), 1539 (C═C aromatic). **^{1}H NMR (400 MHz, DMSO-d_6):** δ 8.88 (s, 1H, NH-C═O, D_2O exchangeable), 8.75 (s, 1H, NH-C═O, D_2O exchangeable), 8.24 (s, 1H, NH, D_2O exchangeable), 8.02−7.98 (m, 3H, Ar−H + H pyridazine), 7.52−7.40 (m, 5H, Ar−H), 7.07 (d, J = 9.3 Hz, 1H, H pyridazine), 6.84 (d, J = 9.0 Hz, 2H, Ar−H), 3.70 (s, 3H, OCH_3). **^{13}C NMR (100 MHz, DMSO):** δ 160.92 (C═O), 156.94, 154.98, 152.78, 137.08, 133.11, 129.32, 129.23, 126.27, 126.21, 121.01, 114.22, 113.84 (Ar−C), 55.59 (OCH_3). **MS:** m/z (%) 335 (M^+, 9), 123 (100). **Anal. Calcd** for $C_{18}H_{17}N_5O_2$ (335.37): C, 64.47; H, 5.11; N, 20.88. Found: C, 64.58; H, 5.27; N, 20.71.

*4.1.6.4. N-(4-Methoxyphenyl)-2-(6-phenylpyridazin-3-yl)-hydrazine-1-carbothioamide (**11d**).* Yield: 75% (0.42 g), mp 178−188 °C. **IR (KBr disk) (cm^{-1}):** 3313,3197, 3128 (NH, NH, NH), 3059−3001 (CH aromatic), 2966- 2835 (CH aliphatic), 1597 (C═N), 1535 (C═C aromatic), 1219 (C═S). **^{1}H NMR (400 MHz, DMSO-d_6):** δ 9.89 (s, 1H, NH-C═S, D_2O exchangeable), 9.78 (s, 1H, NH-C═S, D_2O exchangeable), 9.22 (s, 1H, NH, D_2O exchangeable), 8.08−8.03 (m, 3H, Ar−H+ H pyridazine), 7.52 (t, J = 7.3 Hz, 2H, Ar−H), 7.45 (t, J = 7.3 Hz, 1H, Ar−H), 7.37 (d, J = 8.9 Hz, 2H, Ar−H), 7.02 (d, J = 9.3 Hz, 1H, H pyridazine), 6.88 (d, J = 8.9 Hz, 2H, Ar−H), 3.74 (s, 3H, OCH_3). **^{13}C NMR (100 MHz, DMSO):** δ 182.23 (C═S), 160.17, 157.16, 153.31, 136.94, 132.48, 129.38, 127.83, 127.58, 126.43, 126.31, 114.17, 113.66 (Ar−C), 55.67 (OCH_3). **MS:** m/z (%) 352 (M^+, 7), 228 (100). **Anal. Calcd** for $C_{18}H_{17}N_5OS$ (351.43): C, 61.52; H, 4.88; N, 19.93; S, 9.12. Found: C, 61.34; H, 5.06; N, 20.14; S, 9.26.

*4.1.6.5. N-(4-Chlorophenyl)-2-(6-(3,4-dimethoxyphenyl)-pyridazin-3-yl)hydrazine-1-carboxamide (**11e**).* Yield: 50% (0.33 g), mp 221−223 °C. **IR (KBr disk) (cm^{-1}):** 3332−3209 (NH, NH, NH), 3074 (CH aromatic), 2935- 2908 (CH aliphatic), 1674 (C═O), 1593 (C═N), 1539 (C═C aromatic). **^{1}H NMR (400 MHz, DMSO-d_6):** δ 9.07 (s, 1H, NH-C═O, D_2O exchangeable), 8.83 (s, 1H, NH-C═O, D_2O exchangeable), 8.37 (s, 1H, NH, D_2O exchangeable), 7.98 (d, J = 9.4 Hz, 1H, H pyridazine), 7.66 (d, J = 2.1 Hz, 1H, Ar−H), 7.57 (d, J = 8.6 Hz, 2H, Ar−H), 7.53 (dd, J = 8.6, 2.0 Hz, 1H, Ar−H), 7.29 (d, J = 8.9, 2H, Ar−H), 7.07−7.03 (m, 2H, Ar−H + H pyridazine), 3.84 (s, 3H, OCH_3), 3.81 (s, 3H, OCH_3). **^{13}C NMR (100 MHz, DMSO):** δ 160.37 (C═O), 156.75, 152.66, 150.10, 149.51, 139.25, 129.74, 128.85, 125.90, 125.85, 120.69, 118.79, 114.00, 112.30, 109.54 (Ar−C), 56.01, 55.96 (OCH_3). **MS:** m/z (%) 399 (M^+, 5), 55 (100). **Anal. Calcd** for $C_{19}H_{18}ClN_5O_3$ (399.84): C, 57.08; H, 4.54; N, 17.52. Found: C, 57.24; H, 4.70; N, 17.64.

*4.1.6.6. 2-(6-(3,4-Dimethoxyphenyl)pyridazin-3-yl)-N-phenylhydrazine-1-carbothioamide (**11f**).* Yield: 75% (0.46 g), mp 187−189 °C. **IR (KBr disk) (cm^{-1}):** 3267, 3205, 3143 (NH, NH, NH), 3062−2997 (CH aromatic), 2966−2835 (CH aliphatic), 1600 (C═N), 1550 (C═C aromatic), 1222 (C═S). **^{1}H NMR (400 MHz, DMSO-d_6):** δ 9.97 (s, 1H, NH-C═S, D_2O exchangeable), 9.84 (s, 1H, NH-C═S, D_2O exchangeable), 9.14 (s, 1H, NH, D_2O exchangeable), 8.05 (d, J = 9.4 Hz, 1H, H pyridazine), 7.67 (d, J = 2.2 Hz, 1H, Ar−H), 7.54 (m, 3H, Ar−H), 7.31 (t, J = 7.7 Hz, 2H, Ar−H), 7.14 (t, J = 7.4 Hz, 1H, Ar−H), 7.08 (d, J = 8.4 Hz, 1H, Ar−H), 6.99 (d, J = 9.3 Hz, 1H, H pyridazine), 3.86 (s, 3H, OCH_3), 3.82 (s, 3H, OCH_3). **^{13}C NMR (100 MHz, DMSO):** δ 181.95 (C═S), 159.71, 153.11, 150.22, 149.54, 139.67, 129.59, 128.38, 125.98, 125.31, 118.92, 114.27, 112.35, 109.60 (Ar−C), 56.05, 56.01(OCH_3). **MS:** m/z (%) 381 (M^+, 36), 233 (100). **Anal. Calcd** for $C_{19}H_{19}N_5O_2S$ (381.45): C, 59.83; H, 5.02; N, 18.36; S, 8.40. Found: C, 59.94; H, 5.21; N, 18.62; S, 8.53.

*4.1.6.7. 2-(6-(3,4-Dimethoxyphenyl)pyridazin-3-yl)-N-(4-methoxyphenyl)hydrazine-1-carbothioamide (**11g**).* Yield: 45% (0.3 g), mp 179−180 °C. **IR (KBr disk) (cm^{-1}):** 3267, 3201, 3143 (NH, NH, NH), 3062−3005 (CH aromatic), 2966−2835 (CH aliphatic), 1604 (C═N), 1543 (C═C aromatic), 1222 (C═S). **^{1}H NMR (400 MHz, DMSO-d_6):** δ 9.86 (s, 1H, NH-C═S, D_2O exchangeable), 9.74 (s, 1H, NH-C═S, D_2O exchangeable), 9.11 (s, 1H, NH, D_2O exchangeable), 8.05 (d, J = 9.4 Hz, 1H, H pyridazine), 7.68 (d, J = 2.0 Hz, 1H, Ar−H), 7.56 (dd, J = 8.4, 2.0 Hz, 1H, Ar−H), 7.36 (d, J = 8.6 Hz, 2H, Ar−H), 7.08 (d, J = 8.5 Hz, 1H, Ar−H), 6.98 (d, J = 9.3 Hz, 1H,, H pyridazine), 6.88 (d, J = 8.8 Hz, 2H, Ar−H), 3.86 (s, 3H, OCH_3), 3.82 (s, 3H, OCH_3), 3.74 (s, 3H, OCH_3). **^{13}C NMR (100 MHz, DMSO):** δ 182.24(C═S), 159.79, 157.11, 153.06, 150.21, 149.54, 132.52, 129.61, 127.52, 125.97, 118.91, 114.18, 113.62, 112.35, 109.59 (Ar−C), 56.05, 56.01, 55.66(OCH_3). **MS:** m/z (%) 412 (M^+, 38), 168 (100). **Anal. Calcd** for $C_{20}H_{21}N_5O_3S$ (411.48): C, 58.38; H, 5.14; N, 17.02; S, 7.79. Found: C, 58.50; H, 5.39; N, 17.26; S, 8.01.

4.2. *In Vitro* Antiproliferative Screening against NCI-60 Cell Lines. The synthesized target compounds were screened for their antiproliferative activity against 60 cell lines by the National Cancer Institute (NCI), NIH, Bethesda, Maryland, under the Developmental Therapeutics Program (DTP). This screening uses 60 distinct human tumor cell lines including leukemia, colon, nonsmall cell lung cancer, prostate, CNS, renal, ovarian, breast, melanoma, and renal cell carcinoma. Detailed methods are described on NCI Web site (www.dtp.nci.nih.gov).

4.3. Evaluation of the *in Vivo* Anticancer Activity and Safety of 9e. To evaluate the *in vivo* anticancer activity of **9e**, an Ehrlich ascites carcinoma (EAC) solid tumor animal model was used where EAC cells were withdrawn from the ascitic fluid of a tumor-bearing female mouse. Cells were diluted with sterile phosphate-buffered saline to produce almost 2.5 × 10^6 cells per 0.2 mL that was then injected i.m. in the left thigh of 40 female mice (10 mice per group). When palpable masses of tumors were developed (*app.* = 100 mm^3), treatment was initiated. EAC-bearing mice were randomly divided into the following four groups: (i) Control group where mice received only drug vehicle; (ii) SOR group where mice received sorafenib (LC laboratories) at a daily dose of 30 mg/kg, i.p; (iii) **9e** (15 mg) group were mice received **9e** at a daily dose of 15 mg/kg, i.p.; and (iv) **9e** (30 mg) group were mice received **9e** at a daily dose of 30 mg/kg, i.p. SOR was herein used as a reference drug. The doses were delivered in a 10% Tween 80. Another group of untreated normal mice (n = 5) was included in the present study for comparison with 9e to assess its safety profile. Tumor volumes were measured at equal intervals using a digital caliper, according to the following equation[67]

https://doi.org/10.1021/acsomega.4c05250
ACS Omega 2024, 9, 37310−37329

$$\text{tumor volume}(\text{mm}^3) = \text{length}(\text{mm}) \times [\text{height}(\text{mm})]^2 \times 0.52$$

Sacrifice was performed under anesthesia for all groups after 15 days of starting the treatment protocol. Tumors were excised and collected for further analyses. The safety profile of **9e** was assessed in mice using the indicated doses, where short-term acute signs of toxicity, excitability, and vitality along with mortality were monitored and recorded for a duration of 14 days. Additionally, after sacrifice, multiple organs were harvested for histopathological evaluation in comparison with untreated mice. These organs included livers, hearts, spleens, lungs, intestines, and kidneys. All experimental procedures were carried out in accordance with the National Institutes of Health Guide for the Care and Use of Laboratory Animals and were approved by the Ethical Committee of the Faculty of Pharmacy, The British University in Egypt (EX-2203).

*4.3.1. Histopathological Evaluation of **9e** in Solid Tumors.* Tumors were fixed in 10% formalin and embedded in paraffin for the preparation of histological sections. Staining with hematoxylin and eosin (H&E) was then performed to evaluate the histopathological changes in treated groups versus control. Moreover, the necrotic indices for each group were determined in 10 random fields per section per animal using the Leica application computer analyzer system.

*4.3.2. Evaluation of the Effect of **9e** on JNK1, Cyclin D1, and p53 Gene Expression.* Total RNA was extracted from tumor tissues using a Direct-zol RNA MiniPrep Plus Kit (ZYMO RESEARCH CORP.). The quantity and quality of extracted RNA were assessed afterward by calculating the A260/A280 ratio. SuperScript IV One-Step RT-PCR kit (ThermoFisher Scientific, MA) was then used for reverse transcription (RT) of extracted RNA followed by PCR. 48-well plate StepOne instrument (Applied Biosystems) was used in a thermal profile as follows: 10 min at 45 °C for RT, 2 min at 98 °C for RT inactivation, and initial denaturation by 40 cycles of 10 s at 98 °C, 10 s at 55 °C, and 30 s at 72 °C for the amplification step. After the RT-PCR run, the data were expressed in the cycle threshold (Ct) for the target and housekeeping genes. Values of ΔCt correspond to the relative expression change for each gene of interest compared to that of the housekeeping gene of the same sample. The ΔΔCt value was then obtained by subtracting the ΔCt value of the control group from the ΔCt value of each of the treated groups' samples. The relative quantitation of each target gene (expressed as fold change from control) was performed according to the $2^{-\Delta\Delta Ct}$ method.[68] Primer sequences used were as follows: forward 5′-GAACAGGATTGAGTAGCGGC−3′ and reverse 5′-TCATGATGGCAAGCAATTAGTC-3′ for JNK1 gene; 5′-TAGCAGAGAGCTACAGACTTCG-3′ and reverse 5′-CTCCGTCTTGAGCATGGCTC-3′ for cyclin D1 gene; forward 5′-ATAGGTCGGCGGTTCAT-3′ and reverse 5′-CCCGAGTATCTGGAAGACAG-3′ for p53, forward 5′-CGTCCCGTAGACAAAATGGT-3′ and reverse 5′-TCAATGAAGGGGTCGTTGAT-3′ for GAPDH housekeeping gene.

*4.3.3. Evaluation of the Effect of **9e** on p-JNK-1 Protein Levels.* Excised tumors were homogenized as 10% (w/v) in phosphate-buffered saline. Phospho-JNK-1 concentration was then determined in tissue homogenates using a Phospho-JNK-1 ELISA kit (Abcam), according to the manufacturer's instructions. Optical density was determined at 450 nm by using a microplate reader.

*4.3.4. Evaluation of the Effect of **9e** on c-Jun and c-Fos Protein Levels.* Protein concentrations of c-Jun and c-Fos were detected in tumor tissue homogenates using a mouse c-Jun ELISA Kit (FineTest, China) and mouse c-Fos ELISA Kit (MyBioSource), according to the manufacturers' instructions. Optical density was determined at 450 nm using a microplate reader.

4.3.5. Statistical Analysis. Data are presented as mean ± SD and analyzed by one-way analysis of variance (One-way ANOVA), followed by Tukey's *post hoc* test for multiple comparisons using GraphPad Prism version 8 (GraphPad Software, CA). Values of $P < 0.05$ were considered to be statistically significant.

4.4. Molecular Docking. The ligands were drawn with MarvinSketch,[69] and energy was minimized with OpenBabel software,[70] using the steepest descent method with a convergence criterion of 10^{-6} kcal/mol/Å and 10,000 iterations utilizing MMFF94s for energy evaluation at each step. 3D conformations of Ligands were then prepared by OMEGA 3.0.1.2 of OpenEye software for the docking procedure using FRED.[71] The human JNK1 protein structure (PDB ID: 4L7F) was downloaded from the RCSB Protein Data Bank.[72,73] The protein structure was prepared using two different programs, Make Receptor, a graphical utility of OEDOCKING 3.2.0.2 module of OpenEye software, and AutoDock Tools 1.5.6.[74] For Make Receptor, the box of the search area was determined around **AX13587**, and the cocrystallized ligand (PDB ID: 1 V5) with the default dimensions and a docking constrain with Met111 of the hinge region as a hydrogen bond donor was applied. For AutoDock Vina, the search box was centered on the cocrystallized ligand and assigned a 25 Å box side. The docking experiment was carried out by the FRED application of the OEDOCKING 3.2.0.2 module of OpenEye software and AutoDock Vina using PyRx as a graphical user interface.[75] The docking RMSD was calculated using DockRMSD.[76] PyMOL version 2.5.2 was used to generate the figures.[77]

4.5. Molecular Dynamics Simulations. OpenMM setup utility was used to set up the simulation system.[78] The protein−ligand complex PDB file was cleaned up, the missing atoms were inserted, and hydrogen atoms were added at pH 7.0. The complex was then placed in a cubic water box with a 1 nm padding distance across each axis of the complex molecule. Sodium and chloride ions were added to neutralize the complex and to bring the salt concentration to 0.1 Molar. AMBER 14 force field[79] was utilized to parametrize protein molecules, while the TIP3P-FB model[80] was employed for water molecules. JNK1 crystal structure (PDB ID: **4L7F**) was used for MD simulation in complex with **AX13587** (PDB ID: **1 V5**), and both modes of **9e** were treated by the same parameters. For the three ligands, the generalized Amber force field (GAFF) was used utilizing the RDKit cheminformatics toolkit.[81] Long-range electrostatic interactions were calculated using the Particle Mesh Ewald (PME) method[82] with an error tolerance of 0.0005 for truncating the Ewald summation. The cutoff distance of both PME direct space interactions and Lennard-Jones interactions was set to 1.2 nm. For integrating force equations, a Langevin integrator was used with a step size of 2 fs, a temperature of 310 K, and a friction coefficient of 1 ps^{-1}. For pressure coupling, a Monte Carlo barostat[83] was utilized, with 310 K as the constant temperature, 1 atm as the

https://doi.org/10.1021/acsomega.4c05250
ACS Omega 2024, 9, 37310−37329

constant pressure, and 25 steps as the pressure update frequency. The MD simulations were carried out using the OpenMM 7.4.2 application layer, starting with an energy minimization of 10 kJ/mol as an energy convergence criterion and then 500,000 equilibration steps (1 ns) ending up with a production run of 50 ns. RMSD, RMSF, radius of gyration (R_g), ligand RMSD, and number of hydrogen bonds to the protein were calculated using VMD.[84]

■ ASSOCIATED CONTENT

Supporting Information

The Supporting Information is available free of charge at https://pubs.acs.org/doi/10.1021/acsomega.4c05250.

^{1}H NMR and ^{13}C NMR spectra, NCI Single-dose testing results, and NCI five-dose testing graph and table for compound **9e** (PDF)

■ AUTHOR INFORMATION

Corresponding Authors

Riham F. George − *Pharmaceutical Chemistry Department, Faculty of Pharmacy, Cairo University, Cairo 11562, Egypt*; Email: riham.eskandar@pharma.cu.edu.eg, riham.eskandar@cu.edu.eg

Bassem H. Naguib − *Pharmaceutical Chemistry Department, Faculty of Pharmacy, The British University in Egypt, Cairo 11837, Egypt; Pharmaceutical Organic Chemistry Department, Faculty of Pharmacy, Cairo University, Cairo 11562, Egypt*; orcid.org/0009-0009-7175-2078; Email: bassem.naguib@pharma.cu.edu.eg, bassem.naguib@bue.edu.eg

Authors

Mai M. Shaalan − *Pharmaceutical Chemistry Department, Faculty of Pharmacy, The British University in Egypt, Cairo 11837, Egypt*

Essam Eldin A. Osman − *Pharmaceutical Chemistry Department, Faculty of Pharmacy, Cairo University, Cairo 11562, Egypt*; orcid.org/0000-0002-0768-9862

Yasmeen M. Attia − *Pharmacology Department, Faculty of Pharmacy, The British University in Egypt, Cairo 11837, Egypt*

Olfat A. Hammam − *Pathology Department, Theodor Bilharz Research Institute, Imbaba, Giza 12411, Egypt*

Complete contact information is available at: https://pubs.acs.org/10.1021/acsomega.4c05250

Notes

The authors declare no competing financial interest.

■ ACKNOWLEDGMENTS

The authors would like to acknowledge Amgad Albohy, Ph.D., and Muhammad I. Ismail, M.Sc. for their fruitful discussions about the modeling part as well as Ahmed Aladawy for technical support. We appreciate the assistance of OpenEye Scientific Software Inc. in providing an academic license. We would also like to thank NVIDIA Corporation for donating the Titan Xp GPU, which was used for molecular dynamics simulations. The authors would also like to express their gratitude to the members of the Developmental Therapies Program (DTP) at the National Cancer Institute (NCI), Maryland, for carrying out the NCI-60 Human Tumor Cell Lines studies.

■ REFERENCES

(1) Siegel, R. L.; Miller, K. D.; Fuchs, H. E.; Jemal, A. Cancer Statistics, 2021. *Ca-Cancer J. Clin.* **2021**, *71*, 7−33.

(2) Gao, L.; Wu, Z. X.; Assaraf, Y. G.; Chen, Z. S.; Wang, L. Overcoming anti-cancer drug resistance via restoration of tumor suppressor gene function. *Drug Resistance Updates* **2021**, *57*, No. 100770.

(3) Fletcher, J. I.; Haber, M.; Henderson, M. J.; Norris, M. D. ABC transporters in cancer: More than just drug efflux pumps. *Nat. Rev. Cancer* **2010**, *10*, 147−156.

(4) Hassett, M. J.; Rao, S. R.; Brozovic, S.; Stahl, J. E.; Schwartz, J. H.; Maloney, B.; Jacobson, J. O. Chemotherapy-Related Hospitalization Among Community Cancer Center Patients. *Oncologist* **2011**, *16*, 378−387.

(5) Guo, H.; Zhang, T.; Yu, Y.; Xu, F. Cancer Physical Hallmarks as New Targets for Improved Immunotherapy. *Trends Cell Biol.* **2021**, *31*, 520−524.

(6) Paul, M. K.; Mukhopadhyay, A. K. Tyrosine kinase − Role and significance in Cancer. *Int. J. Med. Sci.* **2012**, *1*, 101−115.

(7) Xie, X.; Gu, Y.; Fox, T.; Coll, J. T.; Fleming, M. A.; Markland, W.; Caron, P. R.; Wilson, K. P.; Su, M. S. S. Crystal structure of JNK3: A kinase implicated in neuronal apoptosis. *Structure* **1998**, *6*, 983−991.

(8) Johnson, G. L.; Lapadat, R. Mitogen-activated protein kinase pathways mediated by ERK, JNK, and p38 protein kinases. *Science* **2002**, *298*, 1911−1912.

(9) Davis, R. J. Signal transduction by the JNK group of MAP kinases. *Cell* **2000**, *103*, 239−252.

(10) Bogoyevitch, M. A.; Kobe, B. Uses for JNK: the Many and Varied Substrates of the c-Jun N-Terminal Kinases. *Microbiol. Mol. Biol. Rev.* **2006**, *70*, 1061−1095.

(11) Ha, J.; Kang, E.; Seo, J.; Cho, S. Molecular Sciences Phosphorylation Dynamics of JNK Signaling: Effects of Dual-Specificity Phosphatases (DUSPs) on the JNK Pathway. *Int. J. Mol. Sci.* **2019**, *20*, 6157.

(12) Katari, S. K.; Natarajan, P.; Swargam, S.; Kanipakam, H.; Pasala, C.; Umamaheswari, A. Inhibitor design against JNK1 through e-pharmacophore modeling docking and molecular dynamics simulations. *J. Recept. Signal Transduction* **2016**, *36*, 558−571.

(13) Wu, Q.; Wu, W.; Fu, B.; Shi, L.; Wang, X.; Kuca, K. JNK signaling in cancer cell survival. *Med. Res. Rev.* **2019**, *39*, 2082−2104.

(14) Kallunki, T.; Deng, T.; Hibi, M.; Karin, M. c-Jun can recruit JNK to phosphorylate dimerization partners via specific docking interactions. *Cell* **1996**, *87*, 929−939.

(15) Chen, T. K.; Smith, L. M.; Gebhardt, D. K.; Birrer, M. J.; Brown, P. H. Activation and inhibition of the AP-1 complex in human breast cancer cells. *Mol. Carcinog.* **1996**, *15*, 215−226.

(16) Bubici, C.; Papa, S. JNK signalling in cancer: In need of new, smarter therapeutic targets. *Br. J. Pharmacol.* **2014**, *171*, 24−37.

(17) Tafolla, E.; Wang, S.; Wong, B.; Leong, J.; Kapila, Y. L. JNK1 and JNK2 oppositely regulate p53 in signaling linked to apoptosis triggered by an altered fibronectin matrix: JNK links FAK and p53. *J. Biol. Chem.* **2005**, *280*, 19992−19999.

(18) Schaafsma, E.; Takacs, E. M.; Kaur, S.; Cheng, C.; Kurokawa, M. Predicting clinical outcomes of cancer patients with a p53 deficiency gene signature. *Sci. Rep.* **2022**, *12*, No. 1317.

(19) Schwabe, R. F.; Bradham, C. A.; Uehara, T.; Hatano, E.; Bennett, B. L.; Schoonhoven, R.; Brenner, D. A. c-Jun-N-terminal kinase drives cyclin D1 expression and proliferation during liver regeneration. *Hepatology* **2003**, *37*, 824−832.

(20) Atmaca, H.; Ilhan, S.; Pulat, Ç. Ç.; Dundar, B. A.; Zora, M. Evaluation of Novel Spiro- pyrrolopyridazine Derivatives as Anticancer Compounds: In Vitro Selective Cytotoxicity, Induction of Apoptosis, EGFR Inhibitory Activity, and Molecular Docking Analysis. *ACS Omega* **2024**, *9*, 23713−23723.

(21) George, R. F.; Fouad, M. A.; Gomaa, I. E. O. Synthesis and cytotoxic activities of some pyrazoline derivatives bearing phenyl pyridazine core as new apoptosis inducers. *Eur. J. Med. Chem.* **2016**, *112*, 48−59.

(22) Rathish, I. G.; Javed, K.; Ahmad, S.; Bano, S.; Alam, M. S.; Akhter, M.; Pillai, K. K.; Ovais, S.; Samim, M. Synthesis and evaluation of anticancer activity of some novel 6-aryl-2-(p-sulfamylphenyl)-pyridazin-3(2H)-ones. *Eur. J. Med. Chem.* **2012**, *49*, 304−309.
(23) Ewies, E. F.; El-Shehry, M. F.; Boulos, L. S. Synthesis of some novel pyridazine derivatives of expected antitumor activity. *Int. J. ChemTech Res.* **2015**, *7*, 2506−2513.
(24) Banoğlu, E.; Şüküroğlu, M.; Ergün, B. Ç.; Baytaş, S. N.; Aypar, E.; Ark, M. Synthesis of the Amide Derivatives of 3- [1- (3-Pyridazinyl) −5-phenyl-1H-pyrazole-3-yl] propanoic Acids as Potential Analgesic Compounds. *Turk. J. Chem.* **2007**, *31*, 677−687.
(25) Ökçelik, B.; Ünlü, S.; Banoglu, E.; Küpeli, E.; Yeşilada, E.; Şahin, M. F. Investigations of new pyridazinone derivatives for the synthesis of potent analgesic and anti-inflammatory compounds with cyclooxygenase inhibitory activity. *Arch. Pharm.* **2003**, *336*, 406−412.
(26) Islam, M.; Siddiqui, A. A.; Rajesh, R. Synthesis, antitubercular, antifungal and antibacterial activities of 6-substituted phenyl-2-(3′-substituted phenyl pyridazin-6′-yl)-2,3, 4,5-tetrahydropyridazin-3-one. *Acta Polym. Pharm.* **2008**, *65*, 353−362.
(27) Asif, M. Some Recent Approaches of Biologically Active Substituted Pyridazine and Phthalazine Drugs. *Curr. Med. Chem.* **2012**, *19*, 2984−2991.
(28) Cignarella, G.; Barlocco, D.; Pinna, G. A.; Loriga, M.; Curzu, M. M.; Tofanetti, O.; Sassari, U.; Muroni, V.; Robin, B. B. Synthesis and Biological Evaluation of Substituted Benzo[h]cinnolinones and 3H-Benzo[6,7]cyclohepta[1,2-c]pyridazinones: Higher Homologues of the Antihypertensive and Antithrombotic 5H-Indeno[1,2-c]pyridazinones. *J. Med. Chem.* **1989**, *32*, 2277−2282.
(29) Akbas, E.; Berber, I. Antibacterial and antifungal activities of new pyrazolo[3,4-d]pyridazin derivatives. *Eur. J. Med. Chem.* **2005**, *40*, 401−405.
(30) Eissa Mohammed, Y. H.; Thirusangu, P.; Zabiulla; Vigneshwaran, V.; BT, P.; Khanum, S. A. The anti-invasive role of novel synthesized pyridazine hydrazide appended phenoxy acetic acid against neoplastic development targeting matrix metallo proteases. *Biomed. Pharmacother.* **2017**, *95*, 375−386.
(31) Garber, K. Cancer anabolic metabolism inhibitors move into clinic. *Nat. Biotechnol.* **2016**, *34*, 794−795.
(32) Horn, L.; Wang, Z.; Wu, G.; Poddubskaya, E.; Mok, T.; Reck, M.; Wakelee, H.; Chiappori, A. A.; Lee, D. Ho.; Breder, V.; Orlov, S.; Cicin, I.; Cheng, Y.; Liu, Y.; Fan, Y.; Whisenant, J. G.; Zhou, Y.; Oertel, V.; Harrow, K.; Liang, C.; Mao, L.; Selvaggi, G.; Wu, Y.-L. Ensartinib vs Crizotinib for Patients With Anaplastic Lymphoma Kinase−Positive Non-Small Cell Lung Cancer A Randomized Clinical Trial. *JAMA Oncol.* **2021**, *7*, 1617−1625.
(33) Huang, W. S.; Metcalf, C. A.; Sundaramoorthi, R.; Wang, Y.; Zou, D.; Thomas, R. M.; Zhu, X.; Cai, L.; Wen, D.; Liu, S.; Romero, J.; Qi, J.; Chen, I.; Banda, G.; Lentini, S. P.; Das, S.; Xu, Q.; Keats, J.; Wang, F.; Wardwell, S.; Ning, Y.; Snodgrass, J. T.; Broudy, M. I.; Russian, K.; Zhou, T.; Commodore, L.; Narasimhan, N. I.; Mohemmad, Q. K.; Iuliucci, J.; Rivera, V. M.; Dalgarno, D. C.; Sawyer, T. K.; Clackson, T.; Shakespeare, W. C. Discovery of 3-[2-(imidazo[1,2- b]pyridazin-3-yl)ethynyl]-4-methyl- N -{4-[(4-methylpiperazin-1-yl)methyl]-3-(trifluoromethyl)phenyl}benzamide (AP24534), a potent, orally active pan-inhibitor of breakpoint cluster region-abelson (BCR-ABL) kinase including the T315I gatekeeper mutant. *J. Med. Chem.* **2010**, *53*, 4701−4719.
(34) Wicker, C. A.; Hunt, B. G.; Krishnan, S.; Aziz, K.; Parajuli, S.; Palackdharry, S.; Elaban, W. R.; Wise-Draper, T. M.; Mills, G. B.; Waltz, S. E.; Takiar, V. Glutaminase inhibition with telaglenastat (CB-839) improves treatment response in combination with ionizing radiation in head and neck squamous cell carcinoma models. *Cancer Lett.* **2021**, *502*, 180−188.
(35) Palmer, W. S.; Alam, M.; Arzeno, H. B.; Chang, K. C.; Dunn, J. P.; Goldstein, D. M.; Gong, L.; Goyal, B.; Hermann, J. C.; Hogg, J. H.; Hsieh, G.; Jahangir, A.; Janson, C.; Jin, S.; Ursula Kammlott, R.; Kuglstatter, A.; Lukacs, C.; Michoud, C.; Niu, L.; Reuter, D. C.; Shao, A.; Silva, T.; Trejo-Martin, T. A.; Stein, K.; Tan, Y. C.; Tivitmahaisoon, P.; Tran, P.; Wagner, P.; Weller, P.; Wu, S. Y. Development of amino-pyrimidine inhibitors of c-Jun N-terminal kinase (JNK): Kinase profiling guided optimization of a 1,2,3-benzotriazole lead. *Bioorg. Med. Chem. Lett.* **2013**, *23*, 1486−1492.
(36) Doma, A.; Kulkarni, R.; Palakodety, R.; Sastry, G. N.; Sridhara, J.; Garlapati, A. Pyrazole derivatives as potent inhibitors of c-Jun N-terminal kinase: Synthesis and SAR studies. *Bioorg. Med. Chem.* **2014**, *22*, 6209−6219.
(37) Li, B.; Cociorva, O. M.; Nomanbhoy, T.; Weissig, H.; Li, Q.; Nakamura, K.; Liyanage, M.; Zhang, M. C.; Shih, A. Y.; Aban, A.; Hu, Y.; Cajica, J.; Pham, L.; Kozarich, J. W.; Shreder, K. R. Hit-to-lead optimization and kinase selectivity of imidazo[1,2-a] quinoxalin-4-amine derived JNK1 inhibitors. *Bioorg. Med. Chem. Lett.* **2013**, *23*, 5217−5222.
(38) Coates, W. J.; McKillop, A. One-Pot preparation of 6-substituted 3(2H)-Pyridazinones from Ketones. *Synthesis* **1993**, *1993*, 334−342.
(39) Kümmerle, A. E.; Vieira, M. M.; Schmitt, M.; Miranda, A. L. P.; Fraga, C. A. M.; Bourguignon, J. J.; Barreiro, E. J. Design, synthesis and analgesic properties of novel conformationally-restricted N-acylhydrazones (NAH). *Bioorg. Med. Chem. Lett.* **2009**, *19*, 4963−4966.
(40) Albrecht, B. K.; Harmange, J. C.; Bauer, D.; Berry, L.; Bode, C.; Boezio, A. A.; Chen, A.; Choquette, D.; Dussault, I.; Fridrich, C.; Hirai, S.; Hoffman, D.; Larrow, J. F.; Kaplan-Lefko, P.; Lin, J.; Lohman, J.; Long, A. M.; Moriguchi, J.; O'Connor, A.; Potashman, M. H.; Reese, M.; Rex, K.; Siegmund, A.; Shah, K.; Shimanovich, R.; Springer, S. K.; Teffera, Y.; Yang, Y.; Zhang, Y.; Bellon, S. F. Discovery and optimization of triazolopyridazines as potent and selective inhibitors of the c-Met kinase. *J. Med. Chem.* **2008**, *51*, 2879−2882.
(41) Botros, S.; Naguib, B. H.; Osman, A. N. Synthesis and tranquilizing effect of new dibenzoxazepines and pyridobenzoxazepines. *Egypt. J. Chem.* **2011**, *54*, 691−701.
(42) Shoemaker, R. H. The NCI60 human tumour cell line anticancer drug screen. *Nat. Rev. Cancer* **2006**, *6*, 813−823.
(43) Szczepankiewicz, B. G.; Kosogof, C.; Nelson, L. T. J.; Liu, G.; Liu, B.; Zhao, H.; Serby, M. D.; Xin, Z.; Liu, M.; Gum, R. J.; Haasch, D. L.; Wang, S.; Clampit, J. E.; Johnson, E. F.; Lubben, T. H.; Stashko, M. A.; Olejniczak, E. T.; Sun, C.; Dorwin, S. A.; Haskins, K.; Abad-Zapatero, C.; Fry, E. H.; Hutchins, C. W.; Sham, H. L.; Rondinone, C. M.; Trevillyan, J. M. Aminopyridine-based c-Jun N-terminal kinase inhibitors with cellular activity and minimal cross-kinase activity. *J. Med. Chem.* **2006**, *49*, 3563−3580.
(44) Zhao, H.; Serby, M. D.; Xin, Z.; Szczepankiewicz, B. G.; Liu, M.; Kosogof, C.; Liu, B.; Nelson, L. T. J.; Johnson, E. F.; Wang, S.; Pederson, T.; Gum, R. J.; Clampit, J. E.; Haasch, D. L.; Abad-Zapatero, C.; Fry, E. H.; Rondinone, C.; Trevillyan, J. M.; Sham, H. L.; Liu, G. Discovery of potent, highly selective, and orally bioavailable pyridine carboxamide c-Jun NH2-terminal kinase inhibitors. *J. Med. Chem.* **2006**, *49*, 4455−4458.
(45) Humphries, P. S.; Lafontaine, J. A.; Agree, C. S.; Alexander, D.; Chen, P.; Do, Q. Q. T.; Li, L. Y.; Lunney, E. A.; Rajapakse, R. J.; Siegel, K.; Timofeevski, S. L.; Wang, T.; Wilhite, D. M. Synthesis and SAR of 4-substituted-2-aminopyrimidines as novel c-Jun N-terminal kinase (JNK) inhibitors. *Bioorg. Med. Chem. Lett.* **2009**, *19*, 2099−2102.
(46) Zhang, T.; Inesta-Vaquera, F.; Niepel, M.; Zhang, J.; Ficarro, S. B.; MacHleidt, T.; Xie, T.; Marto, J. A.; Kim, N.; Sim, T.; Laughlin, J. D.; Park, H.; Lograsso, P. V.; Patricelli, M.; Nomanbhoy, T. K.; Sorger, P. K.; Alessi, D. R.; Gray, N. S. Discovery of potent and selective covalent inhibitors of JNK. *Chem. Biol.* **2012**, *19*, 140−154.
(47) Yang, J. D.; Nakamura, I.; Roberts, L. R. The tumor microenvironment in hepatocellular carcinoma: Current status and therapeutic targets. *Semin. Cancer Biol.* **2011**, *21*, 35−43.
(48) Blonska, M.; Zhu, Y.; Chuang, H. H.; You, M. J.; Kunkalla, K.; Vega, F.; Lin, X. Jun-regulated genes promote interaction of diffuse large B-cell lymphoma with the microenvironment. *Blood* **2015**, *125*, 981−991.

https://doi.org/10.1021/acsomega.4c05250
ACS Omega 2024, 9, 37310−37329

(49) Schröder, S. K.; Asimakopoulou, A.; Tillmann, S.; Koschmieder, S.; Weiskirchen, R. TNF-α controls Lipocalin-2 expression in PC-3 prostate cancer cells. *Cytokine* **2020**, *135*, No. 155214.
(50) Chen, S. Y.; Cai, C.; Fisher, C. J.; Zheng, Z.; Omwancha, J.; Hsieh, C. L.; Shemshedini, L. c-Jun enhancement of androgen receptor transactivation is associated with prostate cancer cell proliferation. *Oncogene* **2006**, *25*, 7212−7223.
(51) Juneja, J.; Cushman, I.; Casey, P. J. G12 signaling through c-jun nh 2-terminal kinase promotes breast cancer cell invasion. *PLoS One.* **2011**, *6*, No. e26085, DOI: 10.1371/journal.pone.0026085.
(52) Chang, M. C.; Chen, C. A.; Chen, P. J.; Chiang, Y. C.; Chen, Y. L.; Mao, T. L.; Lin, H. W.; Lin Chiang, W. H.; Cheng, W. F. Mesothelin enhances invasion of ovarian cancer by inducing MMP-7 through MAPK/ERK and JNK pathways. *Biochem. J.* **2012**, *442*, 293−302.
(53) An, J.; Liu, H.; Magyar, C. E.; Guo, Y.; Veena, M. S.; Srivatsan, E. S.; Huang, J.; QRettig, M. B. Hyperactivated JNK is a therapeutic target in pvhl-deficient renal cell carcinoma. *Cancer Res.* **2013**, *73*, 1374−1385.
(54) Okada, M.; Shibuya, K.; Sato, A.; Seino, S.; Watanabe, E.; Suzuki, S.; Seino, M.; Kitanaka, C. Specific role of JNK in the maintenance of the tumor-initiating capacity of A549 human non-small cell lung cancer cells. *Oncol. Rep.* **2013**, *30*, 1957−1964.
(55) Seino, M.; Okada, M.; Shibuya, K.; Seino, S.; Suzuki, S.; Ohta, T.; Kurachi, H.; Kitanaka, C. Requirement of JNK signaling for self-renewal and tumor-initiating capacity of ovarian cancer stem cells. *Anticancer Res.* **2014**, *34*, 4723−4731.
(56) Bridges, C. S.; Chen, T. J.; Puppi, M.; Rabin, K. R.; Lacorazza, H. D. Anti-leukemic properties of the kinase inhibitor OTSSP167 in T cell acute lymphoblastic leukemia. *Blood Adv.* **2023**, *7*, 422−435.
(57) Blumenschein, G. R.; Gatzemeier, U.; Fossella, F.; Stewart, D. J.; Cupit, L.; Cihon, F.; O'Leary, J.; Reck, M. Phase II, multicenter, uncontrolled trial of single-agent sorafenib in patients with relapsed or refractory, advanced non-small-cell lung cancer. *J. Clin. Oncol.* **2009**, *27*, 4274−4280.
(58) Wang, H. L.; Ma, X.; Guan, X. Y.; Song, C.; Li, G. B.; Yu, Y. M.; Yang, L. L. Potential synthetic lethality for breast cancer: A selective sirtuin 2 inhibitor combined with a multiple kinase inhibitor sorafenib. *Pharmacol. Res.* **2022**, *177*, No. 106050.
(59) Liu, J.; Lin, A. Role of JNK activation in apoptosis: a double-edged sword. *Cell Res.* **2005**, *15* (1), 36−42 Jan.
(60) García-Hernández, L.; García-Ortega, M. B.; Ruiz-Alcalá, G.; Carrillo, E.; Marchal, J. A.; García, M.Á. The p38 MAPK Components and Modulators as Biomarkers and Molecular Targets in Cancer. *Int. J. Mol. Sci.* **2022**, *23* (1), 370 Dec 29.
(61) Tam, S. Y.; Law, H. K. JNK in Tumor Microenvironment: Present Findings and Challenges in Clinical Translation. *Cancers* **2021**, *13* (9), 2196.
(62) OEDOCKING 3.2.0.2; OpenEye Scientific Software: Santa Fe, NM.. http://www.eyesopen.com.
(63) McGann, M. Fred pose prediction and virtual screening accuracy. *J. Chem. Inf. Model.* **2011**, *51*, 578−596.
(64) McGann, M. FRED and HYBRID docking performance on standardized datasets. *J. Comput. Aided. Mol. Des.* **2012**, *26*, 897−906.
(65) Trott, O.; Olson, A. J. AutoDock Vina: Improving the speed and accuracy of docking with a new scoring function, efficient optimization, and multithreading. *J. Comput. Chem.* **2010**, *31*, 455−461.
(66) Cole, J. C.; Murray, C. W.; Nissink, J. W. M.; Taylor, R. D.; Taylor, R. Comparing protein-ligand docking programs is difficult. *Proteins* **2005**, *60*, 325−332.
(67) Mandal, M.; Jaganathan, S. K.; Mondhe, D.; Wani, Z. A.; Pal, H. C. Effect of honey and eugenol on ehrlich ascites and solid carcinoma. *J. Biomed. Biotechnol.* **2010**, *2010*, No. 989163.
(68) Schmittgen, T. D.; Livak, K. J. Analyzing real-time PCR data by the comparative CT method. *Nat. Protoc.* **2008**, *3*, 1101−1108.
(69) Marvin 18.10, ChemAxon.
(70) O'Boyle, N. M.; Banck, M.; James, C. A.; Morley, C.; Vandermeersch, T.; Hutchison, G. R. Open Babel: An open chemical toolbox Noel. *J. Cheminf.* **2011**, *3*, 1−14.
(71) Hawkins, P. C. D.; Skillman, A. G.; Warren, G. L.; Ellingson, B. A.; Stahl, M. T. Conformer generation with OMEGA: Algorithm and validation using high quality structures from the protein databank and cambridge structural database. *J. Chem. Inf. Model.* **2010**, *50*, 572−584.
(72) Berman, H. M.; Westbrook, J.; Feng, Z.; Gilliland, G.; Bhat, T. N.; Weissig, H.; Shindyalov, I. N.; Bourne, P. E. The Protein Data Bank. *Nucleic Acids Res.* **2000**, *28*, 235−242.
(73) Burley, S. K.; Berman, H. M.; Bhikadiya, C.; Bi, C.; Chen, L.; Di Costanzo, L.; Christie, C.; Dalenberg, K.; Duarte, J. M.; Dutta, S.; Feng, Z.; Ghosh, S.; Goodsell, D. S.; Green, R. K.; Guranović, V.; Guzenko, D.; Hudson, B. P.; Kalro, T.; Liang, Y.; Lowe, R.; Namkoong, H.; Peisach, E.; Periskova, I.; Prlić, A.; Randle, C.; Rose, A.; Rose, P.; Sala, R.; Sekharan, M.; Shao, C.; Tan, L.; Tao, Y. P.; Valasatava, Y.; Voigt, M.; Westbrook, J.; Woo, J.; Yang, H.; Young, J.; Zhuravleva, M.; Zardecki, C. RCSB Protein Data Bank: biological macromolecular structures enabling research and education in fundamental biology, biomedicine, biotechnology and energy. *Nucleic Acids Res.* **2019**, *47*, D464−D474.
(74) Morris, G. M.; Ruth, H.; Lindstrom, W.; Sanner, M. F.; Belew, R. K.; Goodsell, D. S.; Olson, A. J. AutoDock4 and AutoDockTools4: Automated docking with selective receptor flexibility. *J. Comput. Chem.* **2009**, *30*, 2785−2791.
(75) Dallakyan, S.; Olson, A. J. Small-molecule library screening by docking with PyRx. *Methods Mol. Biol.* **2015**, *1263*, 243−250.
(76) Bell, E. W.; Zhang, Y. DockRMSD: An open-source tool for atom mapping and RMSD calculation of symmetric molecules through graph isomorphism. *J. Cheminf.* **2019**, *11*, No. 40.
(77) The PyMOL Molecular Graphics Systems, Version 2.5.2, Schrodinger, LLC. https://pymol.org/.
(78) Eastman, P.; Swails, J.; Chodera, J. D.; McGibbon, R. T.; Zhao, Y.; Beauchamp, K. A.; Wang, L. P.; Simmonett, A. C.; Harrigan, M. P.; Stern, C. D.; Wiewiora, R. P.; Brooks, B. R.; Pande, V. S. OpenMM 7: Rapid development of high performance algorithms for molecular dynamics. *PLoS Comput. Biol.* **2017**, *13*, No. e1005659.
(79) Maier, J. A.; Martinez, C.; Kasavajhala, K.; Wickstrom, L.; Hauser, K. E.; Simmerling, C. ff14SB: Improving the Accuracy of Protein Side Chain and Backbone Parameters from ff99SB. *J. Chem. Theory Comput.* **2015**, *11*, 3696−3713.
(80) Wang, L. P.; Martinez, T. J.; Pande, V. S. Building force fields: An automatic, systematic, and reproducible approach. *J. Phys. Chem. Lett.* **2014**, *5*, 1885−1891.
(81) Wang, J.; Wolf, R. M.; Caldwell, J. W.; Kollman, P. A.; Case, D. A. Development and Testing of a General Amber Force Field. *J. Comput. Chem.* **2004**, *25*, 1157−1174.
(82) Essmann, U.; Perera, L.; Berkowitz, M. L.; Darden, T.; Lee, H.; Pedersen, L. G. A smooth particle mesh Ewald method. *J. Chem. Phys.* **1995**, *103*, 8577−8593.
(83) Chow, K. H.; Ferguson, D. M. Isothermal-isobaric molecular dynamics simulations with Monte Carlo volume sampling. *Comput. Phys. Commun.* **1995**, *91*, 283−289.
(84) Humphrey, W.; Dalke, A.; Schulten, K. VMD: Visual molecular dynamics. *J. Mol. Graphics* **1996**, *14*, 33−38.

https://doi.org/10.1021/acsomega.4c05250
ACS Omega 2024, 9, 37310−37329